**TRIBHUVAN UNIVERSITY**

**INSTITUTE OF ENGINEERING**

**PULCHOWK CAMPUS**

**Thesis number: M-53-MSMDE-2019-2022**

# Sediment Erosion in Head Cover Pressure Balancing Pipe – A Case Study of Chameliya Hydroelectric Power Station (CHEPS)

by

Chiranjibi Acharya

A THESIS

SUBMITTED TO THE DEPARTMENT OF MECHANICAL AND AEROSPACE ENGINEERING

IN PARTIAL FULFILLMENT OF THE REQUIREMENTS FOR THE DEGREE OF MASTER OF SCIENCE IN MECHANICAL SYSTEMS DESIGN AND ENGINEERING

DEPARTMENT OF MECHANICAL AND AEROSPACE ENGINEERING

LALITPUR, NEPAL

SEPTEMBER, 2022

## COPYRIGHT

**TRIBHUVAN UNIVERSITY**

**INSTITUTE OF ENGINEERING**

**PULCHOWK CAMPUS**

**DEPARTMENT OF MECHANICAL AND AEROSPACE ENGINEERING**

The undersigned certify that they have read, and recommend to the Institute of Engineering for acceptance, a thesis entitled "**Sediment Erosion in Head Cover Pressure Balancing Pipe - A Case Study of Chameliya Hydroelectric Power Station**" submitted by Chiranjibi Acharya in partial fulfillment of the requirements for the degree of Master in Mechanical Systems Design and Engineering.

_____

Supervisor, Dr. Laxman Poudel
Professor, Department of Mechanical and Aerospace Engineering, Pulchowk Campus, Institute of Engineering, TU

_____

Supervisor, Dr. Sudip Bhattrai
Asst. Professor, Department of Mechanical and Aerospace Engineering, Pulchowk Campus, Institute of Engineering, TU

_____

External Examiner, Er. Madan Timsina
Chief, NEA Subsidiary Company Monitoring Directorate
Nepal Electricity Authority

_____

Committee Chairperson, Dr. Surya Prasad Adhikari
Head, Department of Mechanical and Aerospace Engineering, Pulchowk Campus, Institute of Engineering, TU

Date: _____

## ABSTRACT

The Chameliya Hydropower Plant, located in the Darchula district of Far-Western Province in Nepal has been used as a case study to investigate the erosion caused by sediment in the head cover pressure balancing pipe which has been a significant erosion issue since commissioning. Analyses of erosion have been done by a field study and Computational Fluid Dynamics (CFD) based erosion modeling using a commercial CFD code ANSYS Fluent and the results were compared qualitatively and quantitatively. The sediment concentration (ppm), Particle size distribution (PSD) and Mineral content of the sediment samples were tested. The maximum concentration was found to be 5308.70 ppm on 2021, July 4 and the minimum was 420.20 ppm on 2021, May 3. According to PSD analysis, 90% of the particles (by weight) fall in the range of 0.01 mm to 0.1 mm in the dry month and 0.01 mm to 0.5 mm in the wet month. Despite weather variations, the mineral composition of the silt was seen to be stable, with an average of 70.8% of the minerals being harder than the material of the pressure balance pipe (i.e. Steel SS304). Erosion rate density at respective points (where the thickness were measured) was calculated experimentally as well as using CFD simulation. The location of erosion-prone area was found to be the same as the real-life scenario, and the erosion rate density from the simulation follows the same trend as the experimental value with a deviation (average error) of 69.58%. Additionally, the proposed design's (chamber) erosion rate density was reduced on average by 13.49%. Erosion-prone locations were discovered to be relocated away from the chamber. Larger regions with substantial erosion rate density values were seen close to the downstream bend extrados of two elbows which are easier to replace in case the erosion occurs and pipe starts to leak. So, with shift of location, the pipe can be replaced within short period of time (3 to 4 hours), thus proposed design reduces machine downtime (outage), saving energy for maintenance by around 927 MWh per outage hence increase in generation.

**ACKNOWLEDGMENT**

My profound gratitude and appreciation go out to Prof. Dr. Laxman Poudel and Asst. Prof. Sudip Bhattrai, who oversaw my thesis, for their professional advice, persistent help and ideas when necessary, as well as their consistent encouragement during the research process.

I would like to thank the Institute of Engineering and the Department of Mechanical and Aerospace Engineering for their assistance with my thesis. I would like to express my gratitude to Dr. Surya Prasad Adhikari, Head of the Mechanical and Aerospace Engineering Department at the Pulchowk Campus, for his assistance and leadership. Again, let me express my sincere gratitude and appreciation to Prof. Dr. Laxman Poudel, coordinator of the MSMDE, for providing a wonderful interactive environment for thesis work and to the entire elite committee for their insightful comments and suggestions that helped to make this work more relevant.

I would like to take this opportunity to thank Er. Ashesh Babu Timilsina for his helpful suggestions and guidance throughout the Simulation analysis. I am grateful to the whole Chameliya Hydroelectric Power Station (CHEPS) team for their kind assistance. My sincere appreciation goes out to Er. Pashupati Raj Gautam, Er. Umang Karki, Er. Puran Sob (Plant Chief of CHEPS), Er. Mahesh Neupane and Er. Manoj Bashyal whose dedicated effort and technical assistance enabled me to complete my research objective.

I also want to express my gratitude to the Hydro Lab team for analyzing the sediment samples and giving the necessary information. Last but not least, I'd want to use this chance to convey my profound gratitude and appreciation to my family for their support and ongoing inspiration over the whole duration of my thesis study.

**TABLE OF CONTENTS**

## LIST OF FIGURES

## LIST OF TABLES

## LIST OF ACRONYMS AND ABBREVIATIONS

| | |
|---|---|
| CATIA | Computer Aided Three-Dimensional Interactive Application |
| CFD | Computational Fluid Dynamics |
| CHEPS | Chameliya Hydroelectric Power Station |
| ERD | Erosion rate density |
| GWh | Giga watt hours |
| MVA | Megavolt-Amperes |
| MW | Mega Watt |
| MWh | Megawatt hours |
| NEA | Nepal Electricity Authority |
| PBP | Pressure Balancing Pipe |
| PROR | Peaking Run of River |
| PSD | Particle Size Distribution |

# CHAPTER ONE: INTRODUCTION

## 1.1 Background

High concentrations of feldspar and quartz found in rivers, particularly in the Himalayan basins, have the potential to erode the turbine components of hydroelectric plants (Poudel et al., 2012). The Head Cover and its Pressure Balancing Pipe (PBP), a Francis turbine component, have been affected by significant silt erosion during the monsoon season, resulting in frequent unit shutdowns for maintenance and inconsistent energy generation. Sediment erosion in PBP has been a significant problem for Chameliya Hydroelectric Power Plant (CHEPS) ever since it was commissioned (February 10, 2018). So, a significant step should be taken to address this issue to some extent.

Sand's compositional minerals play a crucial role in characterizing it. Silica, quartz, mica, and feldspar are the most prevalent minerals in sand. Depending on its size, shape, mineral composition, texture, and hardness, sediment can be categorized into several types. The quantity varies depending on the source, the geology of the ground, chemical reactions, use, and additional factors like wind, water transformation, and weather (Poudel et al., 2012). The wear will increase with more sediment content and harder minerals like quartz and feldspar, which have higher hardness values, and this will cause the plant to function below its maximum capacity(Budiarti, 2020). When the particles were large or micrometer-sized, as would be predicted, the erosion rate increased as the particle diameter grew. Similar reasoning applied to flow velocity, where faster flows aided in the erosion process. However, when the particle size shrank, the rate of degradation accelerated. This was explained by the secondary flows at the elbow, which centrifuged the particles toward the walls. The erosion rate for extremely small particles decreased once again when the particle distribution was pointed toward the pipe wall because their low mass was insufficient to erode the pipe wall (Kosinska et al., 2020). Various particle sizes lead to various erosion patterns in the injection mechanism. Although the smaller particles may follow the streamlines and wear the needle tip abrasively, the larger particles had more inertia and were thus more likely to strike the upstream region of the needle orifice (Chongji. Zeng. et al., 2015). The rate and location of erosion may be greatly affected by particle impact velocity and bend radius. (Mazumder et al., 2015).

In multiphase flow, carbon steel 90° elbows are susceptible to erosion/corrosion, particularly for abrasive slug flows. The results demonstrate that erosion/corrosion magnitude increases considerably as concentration levels grow. The concentration of 10 weight percent sand fines in carrier phase enhances the erosion/corrosion rate of carbon steel by up to 93% in comparison to the concentration of 2 weight percent sand fines in slug flow(Khan et al., 2020). Erosion typically happens in the extrados of the pipe bend. The pipe bend type has an impact on the variations that have been observed, the increase in bend curvature directly correlates with an increase in erosion rate (Lospa et al., 2019).

### 1.2 Introduction to Chameliya Hydroelectric Power Station (CHEPS)

CHEPS located in Balanch, Darchula, Sudurpashchim province, is a daily peaking run-of-river (PROR) scheme with a 30 MW installed capacity. On February 10, 2018, the CHEPS was formally inaugurated. Table 1.1 summarizes the salient features of the CHEPS.

Table 1.1: Salient features of CHEPS (NEA 2022)

| | |
|---|---|
| Type | Peaking run off river (6 hour daily peaking) |
| Gross head/ Net head | 103.7 meter/ 94.0 meter |
| Turbine | 2 vertical shaft Francis Runner |
| Installed capacity | 15.6 MW × 2 |
| Rated speed | 428.6 rpm |
| Penstock | Concrete lined and steel lined |
| Generator | 2/3 phase synchronous, rated output 2*16.2 MVA |
| Transformer | 2 × 16.7 MVA (11/132 kV) |
| Annual average energy (Designed) | 184.21 GWhr |
| Catchment area | 85 $km^2$ |
| Mean annual discharge | 46.6 $m^3/s$ |
| Design discharge | 36 $m^3/s$ |
| Design flood discharge | 710 $m^3/s$ |

## 1.3 Problem Statement

Since its commissioning, the CHEPS has been hampered by repeated unit shutdowns caused by significant Sediment erosion, which occurs primarily during the wet seasons. The problem is more pronounced in case of PBP. Primarily on the lower elbow, which is embedded with Headcover. With monsoon season, the sediment loading in river increases, this causes the erosion of elbow, pipe and fittings of the PBP. As a result of this problem, the plant experiences significant energy loss due to unit tripping, which leads to an increase in the cost of repair and maintenance as well as generation loss. Combined it is a significant economic loss for the plant. As a result, alternative methods should be employed to solve this challenge.

## 1.4 Rationale of the Study

Hydropower plants installed in Himalayan originating rivers are significantly affected by sediments which are primarily hard minerals like quartz, feldspar etc. Despite desanding arrangements, small sizes of sediments pass through the generating equipment causing erosion and hence reduced efficiency and high leakages.

In this study, erosion of one of the component of head cover of Francis turbine, the depressurizing pipe (also called PBP) is considered for study. It serves to relieve excessive water pressure leaking from the tip gap between the upper crown of the Francis runner and the inner circle of the Head cover and is generally located in the upward part of the Head cover. The leaking water has a high pressure and whirling motion, causing a massive upward thrust on the Head cover. To reduce the force on the Head cover, a PBP is employed to relieve the leakage water's excessive pressure. This exiting water causes damage of the elbow, coupling flanges of the PBP. This study aims to study the erosion in PBP by field visit and CFD modeling then, proposing alternatives for minimizing the erosion rate. With alternative implementation, it is expected that the frequency of failure decreases with subsequent decrease in tripping due to damage of PBP hence increased generation.

## 1.5 Objectives

### 1.5.1 Main Objective

To study Sediment erosion in Head cover pressure balancing pipe of Chameliya Hydroelectric Power Station.

### 1.5.2 Specific Objectives

- To perform Qualitative and Quantitative analysis of Head cover pressure balancing pipe of CHEPS through field visit.
- To predict the Erosion pattern and Erosion rate density using ANSYS Fluent software.
- To compare the ANSYS simulation result (erosion rate density) with the result obtain from field measurement.
- To propose a design for erosion mitigation.

## 1.6 Limitations

- Cavitation's existence in the flow domain was neglected. Thus, the effect of the sediment particles will be the only cause of the mass loss.
- Since water is considered to be an incompressible fluid, there won't be any density changes. So ANSYS Fluent's pressure-based solver is assumed.
- The sediment concentration data of peak sediment containing month May 3$^{rd}$, August 2$^{nd}$ was only considered.
- After colliding with a solid wall or another particle, the particles remain intact and do not degrade.
- Erosion-related geometry change is neglected.

# CHAPTER TWO: LITERATURE REVIEW

## 2.1 Francis Turbine and It's Components

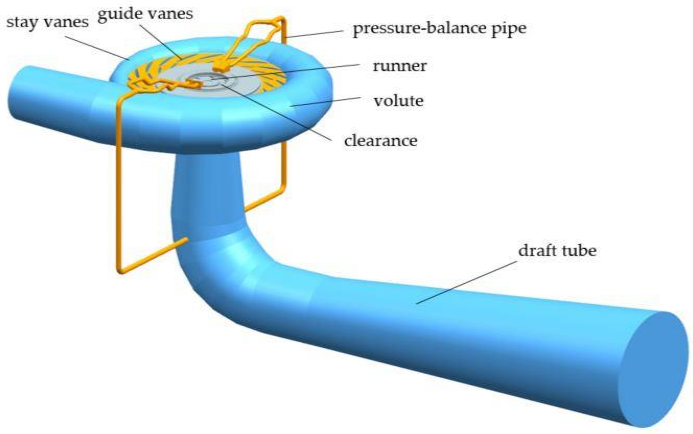


Figure 2.1: Francis Turbine with its components (F. Zhang et al., 2021).

### Spiral Casing

In order to generate the necessary response for the runner to function better, water's kinetic and potential energy are distributed evenly through spiral casing (Dahal et al., 2019).

### Francis runner

Francis runner is a combined axial and radial flow reaction turbine with inward flow. Francis turbines, now the most widely used kind of water turbine. At least in the context of Nepal, Francis turbine design and construction have significantly more difficulties than other types of turbines. Being site-specific, it requires a specialized design to adhere to the site's requirements (Baidar et al., 2015).

### Guide Vanes (Wicket Gates)

To enhance or reduce the flow rate through the turbine, the number of blades on the guiding vanes can be changed. The vanes are positioned between two parallel covers that are normal to the turbine shaft.

### Draft Tube

A hydro turbine's draft tube is an essential component since it allows for a negative head, which raises the turbine's total head. It is underneath the runner and allows flow slowing during departure.

## 2.2 Headcover with Pressure balancing pipe (PBP)

Pressure balancing pipe is located at the upper section of the Headcover and serves to relieve excessive water pressure leaking from the tip gap between the upper crown of the Francis runner and the inner circle of the Headcover. The leaking water has a high pressure and whirling motion, causing a massive upward thrust on the Headcover. To reduce the force on the Headcover, a PBP is employed to relieve the leakage water's excessive pressure. Here, Figure 2.2 shows the lower elbow embedded with headcover and Figure 2.3 shows the elbow and pipes fitting with flanges.

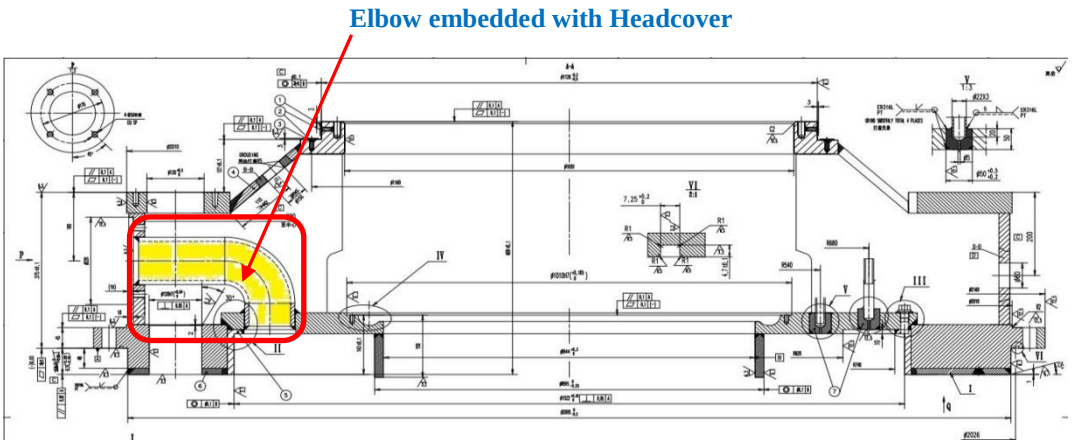


Figure 2.2: Headcover with PBP (NEA, CHEPS)

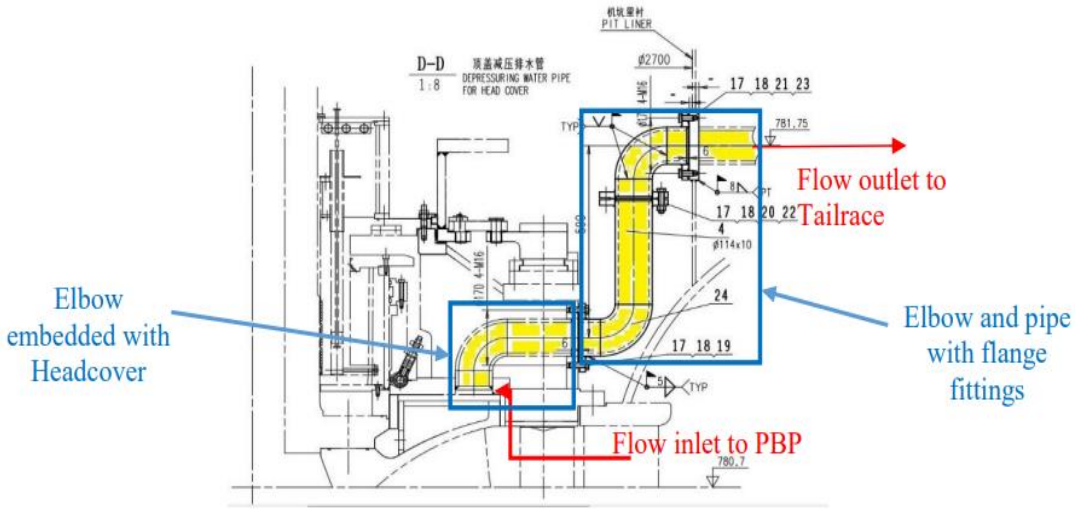


Figure 2.3: Details of PBP (NEA, CHEPS)

## 2.3 Elbow Erosion

### 2.3.1 Solid Particle Erosion Theory

Erosion wear is the material loss brought on by the repeatedly hitting on wall surface with solid particles. It causes major economic losses in a number of industries, including as oil and gas, hydraulic transportation, and chemical processes (Andrews, 1981).

The quantity of particles impacting the surface, their velocity, and their direction in relation to the surface should all affect how quickly an abrasive particle in an inert fluid erodes the surface. These values are heavily influenced by flow conditions, and there are several actual instances when altering flow conditions significantly increased or decreased erosion (Finnie, 1960). Sand erosion of equipment and pipelines is a significant issue for the industry, and it is crucial to study it since it reduces the estimated lifetime of piping systems and is relevant in risk management studies (Srinivasan & Ph, 2014).

It is well known that particles cause wear and financial losses, but do all materials experience this phenomenon? There are differences in the wear mechanisms for brittle and ductile materials. If the surface material is ductile, repeated particle impacts will cause the creation of craters and platelets on the surface. Because platelets eventually become easily eliminated by the flow, craters will grow as a result of the repeated particle impacts. On the other hand, brittle material will experience lateral and radial cracks in response to the impact of sand particles. These cracks will propagate and eventually form small parts that will be destroyed by repeated solid particle impingement. Since the erosion phenomenon differs from case to case, a model that works well in one circumstance might not work as well in another. The phenomenon has been studied (Aquaro & Fontani, 2001).

Particle velocity and impact angle—the angle between the particle and the target surface—were identified as the primary factor of erosion rate in earlier studies. Additionally, it was shown how a variety of elements (including concentration, particle size and shape, abrasive to goal hardness ratio, and the effects of liquid and solid additives) may change the nature and result of the erosion process (Kleĭs & Kulu, 2008).

Sand production is concerning since it might lead to a variety of problems. Erosion, pressure loss, and pipe blockage in particular stand out from the others. In the latter, material is removed from the pipeline through a challenging mechanical process as a result of repetitive sand particle hits. The pipeline may so degrade as a result. Deteriorated pipes may cause pipeline failures that cause both financial losses and environmental issues. Understanding the factors that affect erosion and how to model it are critical. The current research analyzes the erosion equations currently in use and describes the key factors that affect erosion. Additionally, oil and gas industries analyze empirical and mechanistic strategies for pipeline erosion prediction. (Parsi et al., 2014).

In hydro turbines, the effects of erosion wear include altered blade profiles, increased vibration, fatigue damage, ineffective operation, and system failure. The equipment or component that is exposed to and sensitive to the erosive environment may need to be replaced or repaired on a frequent basis, making the erosion damage potentially severe and extremely expensive. (McLaury et al., 1997).

The study of solid particle erosion has successfully made use of computational fluid dynamics (CFD). Particle erosion modeling is one of several multiple aspects of the CFD - based erosion prediction process, along with flow modeling, particle - fluid interaction, particle - particle interaction, and particle - wall interaction (Lospa et al., 2019) and (L. Zhang et al., 2020).

### 2.4 Erosion Model

The erosion phenomenon is studied either theoretically or experimentally. Theoretical study provided mathematical formulae that define erosion as mass of wall material loss per unit mass of particles or mass loss with function of time, whereas experimental studies provide empirical relations. Deriving the theoretical models involves using dimensional analysis or energy balance for particle-target wall collisions. Finnie 1960 first developed a mathematical model for prediction of erosion rate quantitatively by classifying the material as brittle or ductile. Under the hypothesis that brittle materials erode by the form of radial fissures and ductile materials erode by plastic deformation, he provided the following equations to predict the amount of wall material lost by the impact of single abrasive particle.

$$\varepsilon_{VP} = \frac{m_p V_p^2}{P\varphi_k}\left(\sin(2\alpha) - \frac{6}{k}\sin^2(\alpha)\right) \text{ for } \tan(\alpha) \leq \frac{k}{6}$$

$$\varepsilon_{VP} = \frac{m_p V_p^2}{P\varphi_k}\left(\frac{k}{6}\cos^2(\alpha)\right) \text{ for } \tan(\alpha) \geq \frac{k}{6}$$

Equation 2.1

In 1963, Bitter proposed that erosion is caused by two distinct mechanisms: repetitive deformation and cutting. Both erosion owing to cutting wear and erosion due to repetitive deformation are documented in (Bitter, 1963a) and (Bitter, 1963b), respectively. The overall erosion of the target wall is determined by adding (or superimposing) the erosion projected by the two processes.

*Erosion due to deformation,*

$$\varepsilon_{VP} = \frac{1M(V_p sin\alpha - K)^2}{2\delta}$$

*Erosion due to cutting,*

$$\varepsilon_{VC} = \frac{2MV_p(V_p sin\alpha - K)^2}{(V_p sin\alpha)^{\frac{1}{2}}}\left\{V_p cos\alpha - \frac{C(V_p sin\alpha - K)^2}{(V_p sin\alpha)^{\frac{1}{2}}}\chi\right\} for\ \alpha \geq\ \alpha_{P0}$$

Equation 2.2

$$\varepsilon_{VC} = \frac{\frac{1}{2}M\left[V_p^2 cos^2(\alpha) - K_1(V_p sin\alpha - K)^{\frac{3}{2}}\right]}{\chi} for\ \alpha \leq\ \alpha_{P0}$$

Theoretically, cutting wear is caused by the parallel component of the particle's velocity, while deformation wear is caused by the normal component, hence two equations were developed to estimate erosion for large and small angles of attack (Neilson & Gilchrist, 1968).

$$\varepsilon_V = \frac{\frac{1}{2}M\left[V_p^2\cos^2(\alpha) - (V_r)^2\right]}{\chi} + \frac{\frac{1}{2}M\left[(V_p\sin\alpha - K)^2\right]}{\delta} \text{for } \alpha <\ \alpha_{P0}$$

$$\varepsilon_V = \frac{\frac{1}{2}M\left[V_p^2\cos^2(\alpha)\right]}{\chi} + \frac{\frac{1}{2}M\left[(V_p\sin\alpha - K)^2\right]}{\delta} \text{for } \alpha >\ \alpha_{P0}$$

Equation 2.3

The first component in the equation above reflects erosion brought on by cutting, while the second term represents erosion brought on by deformation.

The erosion rate on various materials is assessed using direct impingement testing. Thus, the Erosion/Corrosion Research Center (E/CRC) proposed a number of erosion models based on the direct impingement testing. The model takes into account the direct relationship between erosion and particle velocity and erosion angle. For the prediction of erosion rate on wall surface due to impingement of sand particles flowing with water, a model was created by McLaury et al. in 1997 (McLaury et al., 1997), which is shown below in Equation 2.4.

$$E = AV^n f(\gamma); A = FBh^k \qquad \text{Equation 2.4}$$

Where,

$F$ = Empirical Constant,

$V$ = Impact velocity of particles,

$B_h$ = Hardness number of wall material (Brinell's hardness number),

$k$ = Constant that depends on the wall's construction materials.

Oka et al. proposed an erosion model that takes into consideration the mechanical properties of both the wall material and the impinging particle material normal and any angle of impact (Oka et al., 2005) and (Oka & Yoshida, 2005), which is defined by Equation 2.5.

Erosion occuring at normal impact angle,

$$\varepsilon_{90} = K_p(k_4 H_v)^{k_1 b}\left(\frac{V_p}{v'}\right)^{k_2}\left(\frac{d_p}{d'}\right)^{k_3} \qquad \text{Equation 2.5}$$

Erosion occuring at any impact angle,

$$\varepsilon_\alpha = f(\alpha)\varepsilon_{90}$$

Where,

$K$, $k_1$, $k_2$, $k_3$ are constants depending upon the materials of wall and impinging particle.

Equation 2.6 defines the erosion rate in Fluent Generic model (ANSYS Inc, n.d.), (ANSYS Inc, 2013).

$$R_{erosion} = \sum_{p=1}^{N_{particles}} \frac{\dot{m}_p C(d_p) f(\gamma) v^{b(v)}}{A_{face}} \qquad \text{Equation 2.6}$$

Where,

$C(d_p)$ = Particle diameter function,

$f(\gamma)$ = Dimensionless function of impact angle $\gamma$,

$v$ = Particle impact velocity,

$b(v)$ = Function of particle impact velocity

$A_{face}$ = Cell area facing the wall.

Table 2.1: Major feature of erosion models

| S.N. | Erosion Model | Equation | Major Feature |
|---|---|---|---|
| 1 | Finnie | $E = kV_p^n f(\gamma)$ | More suited for ductile materials |
| 2 | Oka | $E = E_{90}(\frac{V}{V_{ref}})^{k_2}(\frac{d}{d_{ref}})^{k_3} f(\gamma)$ | Correlation that is more realistic by taking into account the influence of wall material hardness |
| 3 | McLaury | $E = AV^n f(\gamma); A = FBh^k$ | Predict the rate at which sand particles in water erode. Slurry viscosity considered |
| 4 | Fluent Generic | $R_{erosion} = \sum_{p=1}^{N_{particles}} \frac{\dot{m}_p C(d_p) f(\gamma) v^{b(v)}}{A_{face}}$ | Other erosion models can be incorporated into ANSYS Fluent by proper deduction |

Among these erosion models McLaury erosion model is used for the study.

## 2.5 CFD Theory

### Computational Fluid Dynamics

The area of computational fluid dynamics is known for simulating flow-related issues using computer resources. A flow problem must be modeled using mathematical, physical, and computational techniques, after which data is produced and reviewed. The flow of fluids is governed by partial differential equations (PDE) that represent the conservation laws for mass, momentum, and energy. Computational fluid dynamics is the practice of replacing such PDE systems with a set of algebraic equations that can be resolved by a computer (CFD). CFD offers a qualitative (and frequently even a quantitative) prediction of fluid flows through the use of mathematical modeling, numerical methods, and software tools.

There are several CFD solution techniques. Among these, finite volume and finite elements are most often utilized. The region to be examined is split into small control volumes using the finite volume approach. The equations are now discretized so that they may be solved repeatedly for each control volume. The finite element approach is another kind, and it is frequently used to study and resolve issues with hydraulic machinery, stress and strain, dynamic response, and eigenvalue analysis. In this method, the area to be analyzed is split into a limited number of elements.

### Governing Equations

ANSYS Fluent resolves the mass and momentum conservation equations for all flows. Additionally, unique conservation equations are computed based on the circumstances. The relevant governing equations in this situation are:

- Mass, Momentum and Energy conservation equations
- Turbulence model: Realizable k-epsilon model
- Particle motion equations for Euler-Lagrange approach

### Pre-Processor

The tasks in the pre-processing stage of problem analysis, which is the first phase, include:

- Creation of geometry
- Generation of mesh/ grid

- Physics and Fluid Properties selection
- Specification of Boundary Conditions

**Solver**

Three distinct streams of numerical solution techniques are; finite difference, finite element, and spectral approaches. The most often used solvers are FLUENT, CFX, and POLYFLOW. Both FLUENT and CFX were separately created by ANSYS, with considerable parallels and differences. Fluent solver employs finite volume for domain discretization whereas CFX solver uses finite elements. The steps used to solve the governing equation of problem are;

- Initialization
- Solution Control
- Monitoring Solution
- Monitoring Convergence

ANSYS Fluent solver (finite volume method) is employed in this study.

**Post-Processor**

Following the use of a solver, the output is then analyzed using contour plots, vector plots that are streamlined, and rendering for graphical representation of the outcome. Viewable results include the ones below. Certain of them are:

- Vector Plots
- X-Y Graph
- Contours
- Particle Tracking
- Discrete particle variables etc.

**Turbulence Modeling in CFD**

The complex fluid motion and unpredictable nature of turbulence make a full analysis quite challenging. The following are the most often used turbulence models in CFD analysis:

- k - epsilon (k-ε) model
- k - omega (k-ω) model
- Shear-Stress Transport (SST) k-ω Model

ANSYS by Launder and Spalding Engineering flow has generally used the fluent standard k-ε model. k- ε, k- ω, and SST turbulence models are the most often used models in CFD to simulate mean flow characteristics for turbulent flow situations. For maximal erosion and dispersion throughout the pipe, the k- ε turbulence model provides closer data than the others, but the SST and k- ω models also exhibit accurate prediction.

### 2.6 Sediment Properties

The following are the most typical sediment qualities studied:

1. Particle Size Distribution (PSD)
2. Minerals content analysis
3. Sediment shape and Sediment concentration analysis

#### Particle Size Distribution (PSD)

The range of particle sizes and their amounts in a specific sample of grains or solids suspended in a fluid medium are referred to as PSD (slurry). Understanding a slurry's PSD is crucial for comprehending its physical and chemical characteristics. From the research already mentioned, it is clear that a major factor contributing to solid particle erosion is the existence of solid sediments in fluid.

#### Minerals Content Analysis

The mineral composition of the silt in rivers is another crucial criterion. One of the most crucial factors in determining a mineral's potential for erosion is its hardness. Different minerals have varying degrees of hardness (Neopane & Sujakhu, 2013) and different shape (Poudel et al., 2012). According to Mohr's hardness scale, the most common mineral in river sediment is quartz, which has a Mohr hardness of 7 and is easily capable of causing turbine erosion. Other minerals that are harder than turbine materials include feldspar, garnet, tourmaline, etc., but mica, which is found in Nepalese river sediments, is softer than turbine material (Neopane & Sujakhu, 2013).

#### Sediment Shape and Sediment concentration analysis

The shape of sediment particles is measured using a variety of criteria, including size, form, flatness, sphericity, elongation, and roundness. To reproduce the sediment morphology, microscopic examination and computer picture processing are typically utilized. Characterizing the morphology of a sediment is an extremely challenging and

time-consuming operation. The dry weight of the sediment to the combined weight of the water and the sediment is known as the sediment concentration and its unit is parts per million (ppm).

## CHAPTER THREE: METHODLOGY

This chapter describes the methodology that is to be opted to apply for the work from start of the thesis till the completion. The methodology followed during the process of thesis is mainly sub divided into different phases as shown in Figure 3.1. The pressure at the inlet and outlet was measured during the field inspection and measurement. The numerical modeling of flow was then performed using the measured data. ANSYS Fluent was used to simulate the flow domain using steady state pressure-based flow model. A sediment sample was taken from the Chameliya HPP, and its PSD curve, mineral content analysis, and sediment concentration analysis were all carried out. In order to predict erosion using the McLaury erosion model, the validated flow model was then updated using the PSD Curve, sediment concentration with discrete phase flow model. The thickness of the eroded elbow and the erosion-prone region were measured and studied, and the results were compared with those from a CFD simulation.

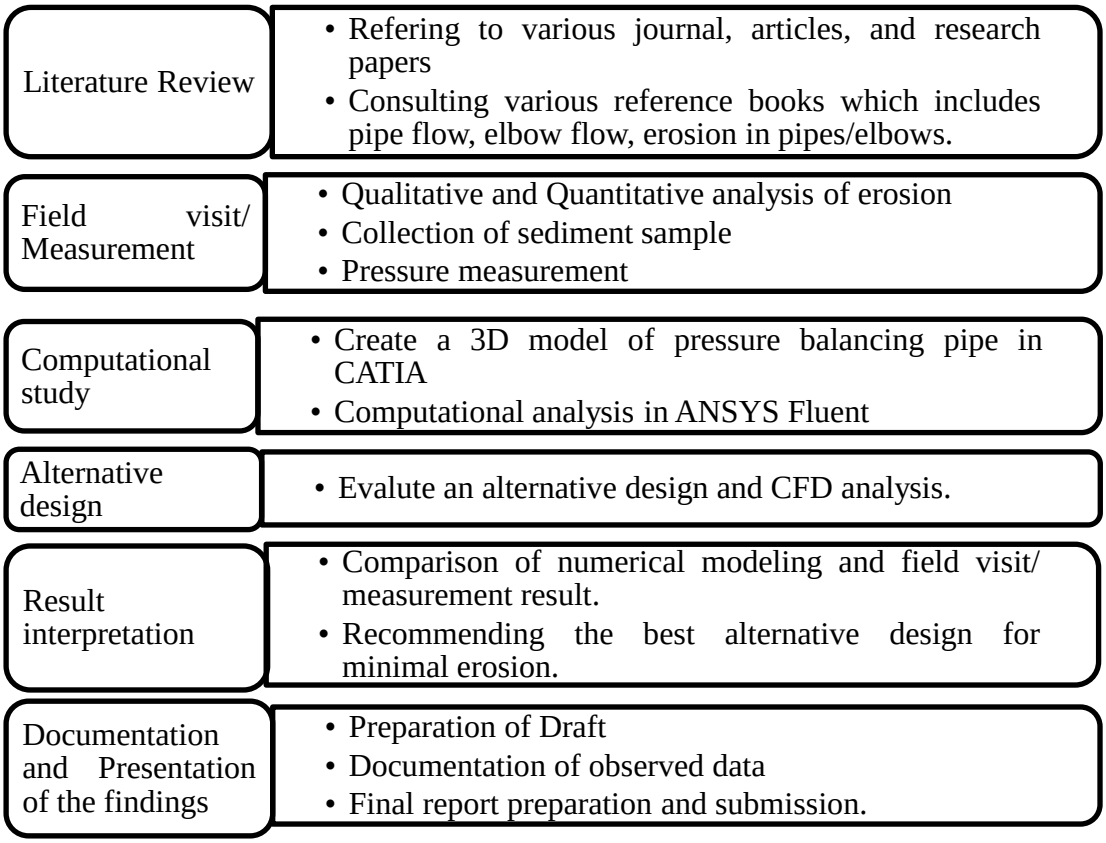


Figure 3.1: Flow diagram of Methodology

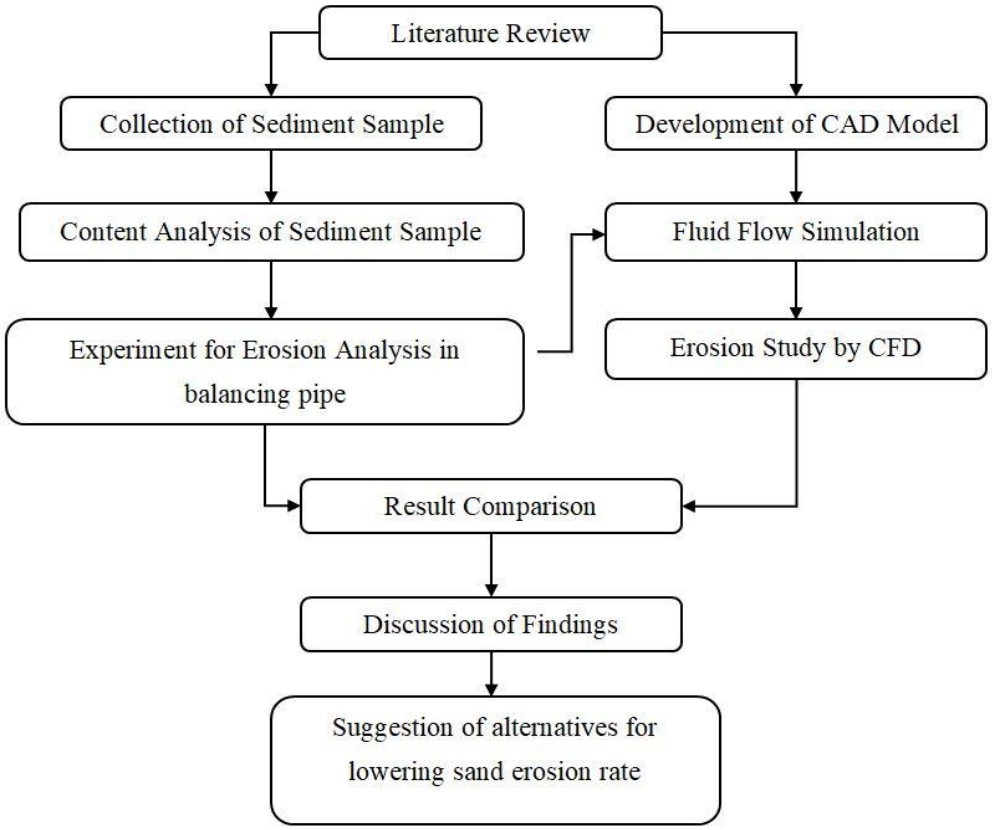


Figure 3.2: Flow chart of Methodology

### 3.1 Literature Review

The literature review covers the majority of the research. Throughout the endeavor, a variety of books, journals, papers, and articles were carefully reviewed and analyzed. The results of earlier studies and research on sediment erosion and possible solutions were studied. To get the necessary background information for the study, it was vitally important to prioritize the literature concentrating on the Sediment erosion rate in PBPs, flow in pipes and elbows, various erosion models, particularly the McLaury erosion model, CATIA, ANSYS Fluent, etc.

### 3.2 Field Visit/ Measurement

A visit was conducted to the Chameliya Hydroelectric Power Station. During the visit the measurement was done on the following processes.

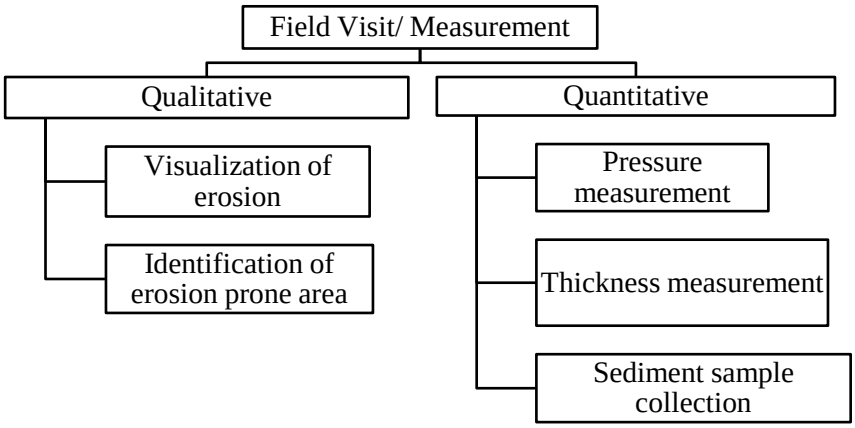


Figure 3.3: Procedure used for field measurement

### 3.2.1 Qualitative measurement

The PBP's erosion was visualized, and at that time, a picture of the eroded elbow was taken. The snapshot collected allowed for the identification of the erosion-prone location.

### 3.2.2 Quantitative measurement

The dimension of existing PBP was measured. During the Unit's full load condition, the fluid pressure at the PBP's intake and outflow sections was also measured. The thickness of the excessively eroded elbow was then measured using a Vernier caliper on several sections, and the loss thickness was taken into account for the study.

| | |
|---|---|
|  |  |
| Inlet gauge pressure = 0.15 MPa | Outlet gauge pressure = 0 MPa |



Figure 3.4: Pressure Measurement

Only the lower elbow (elbow embedded with headcover) which was found excessively eroded through visual inspection during field visit was taken for thickness

measurement. The thickness of the excessively eroded elbow (elbow embedded with headcover) was then measured using a Vernier caliper on several sections, and the loss thickness was taken into account for the study

### 3.2.2.1 Thickness measurement

The Vernier caliper was employed to measure the elbow's thickness at various locations and loss of thickness at each location was calculated by using Equation 3.2. When measuring the thickness, the Vernier caliper's least count was 0.02mm. Uncertainty error also calculated by using Equation 3.1. Below is an explanation of the error analysis and loss of thickness calculation

Error percentage in thickness

$$\sigma_t = \frac{LC}{t} \times 100 \qquad \text{Equation 3.1}$$

Where,

$\sigma_t = percentage\ error\ in\ measurement\ of\ thickness$

$LC = least\ count\ of\ vernier\ caliper$

$t = thickness\ measured\ by\ vernier\ caliper$

Loss of thickness calculation

$$\Delta t = Design\ thickness - t \qquad \text{Equation 3.2}$$

Where,

$Design\ thickness = 10\ mm$

### 3.2.2.2 Erosion rate density calculation from field measurement

The erosion rate (where corrosion rate is neglected) in kg/m$^2$s was calculated by using the following formula (Khan et al., 2019).

$$Erosion\ rate\ (ERD) = \frac{(Initial\ mass - Final\ mass)}{Impact\ Area\ \times Running\ time} = \frac{m}{AT} \qquad \text{Equation 3.3}$$

Where,

$ERD = erosion\ rate\ density$

$m = eroded\ mass\ of\ wall\ material$

$A = Impact\ area\ of\ eroded\ portion$

$T = total\ erosion\ time$

Equation 3.4 was used to calculate erosion rate density at various places once thickness loss was identified, where the total erosion time (T) was taken to be 3 months of the wet season.

For small portion of erosion

$$ER = \frac{\Delta m}{\Delta A \times T} = \frac{\rho \times \Delta t}{T} \qquad \text{Equation 3.4}$$

Where,

$\rho = density\ of\ wall\ material$

$\Delta t = loss\ of\ thickness$

#### 3.2.2.3 Sediment sample collection

Sediment concentration (ppm), Particle size distribution and Mineral content in the inflowing water was tested at Hydro Lab Pvt. Ltd., Lalitpur, Nepal by sampling the flow (incoming to the turbine) on various dates during the rainy season. The results of sediment samples is mentioned in APPENDIX A, B & C.

### 3.3 Computational Study for Existing system

The computational study for the existing PBP system were done on the following steps.

#### 3.3.1 3D Geometry creation

The 2D drawing was created in CATIA V5 and then it was transferred into 3D. Here the dimensions are in millimeter and the elbow is the short radius elbow having 95mm internal diameter with 10mm thickness, which has the radius of bend is same as its nominal diameter.

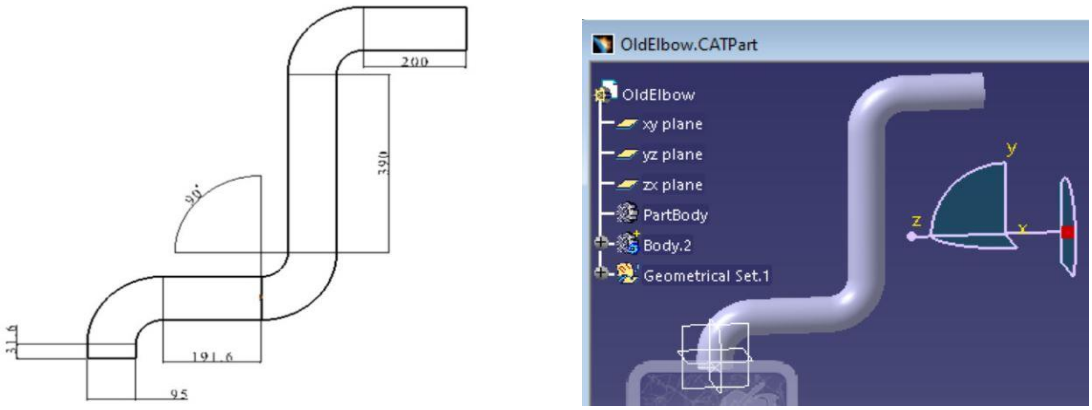


Figure 3.5: 2D and 3D CATIA drawing of existing PBP

### 3.3.2 Meshing

For mesh generation, the 3D geometry of an existing PBP was imported into ANSYS Fluent 21. The 3D domain as a whole was used to construct the mesh. To capture the impact of a sudden shift in flow direction, a fine mesh was utilized on the elbow with an O-grid tropology. Additionally, the inflation layer was utilized close to the wall to capture the effects of the viscous layer (boundary layer) on fluid flow.

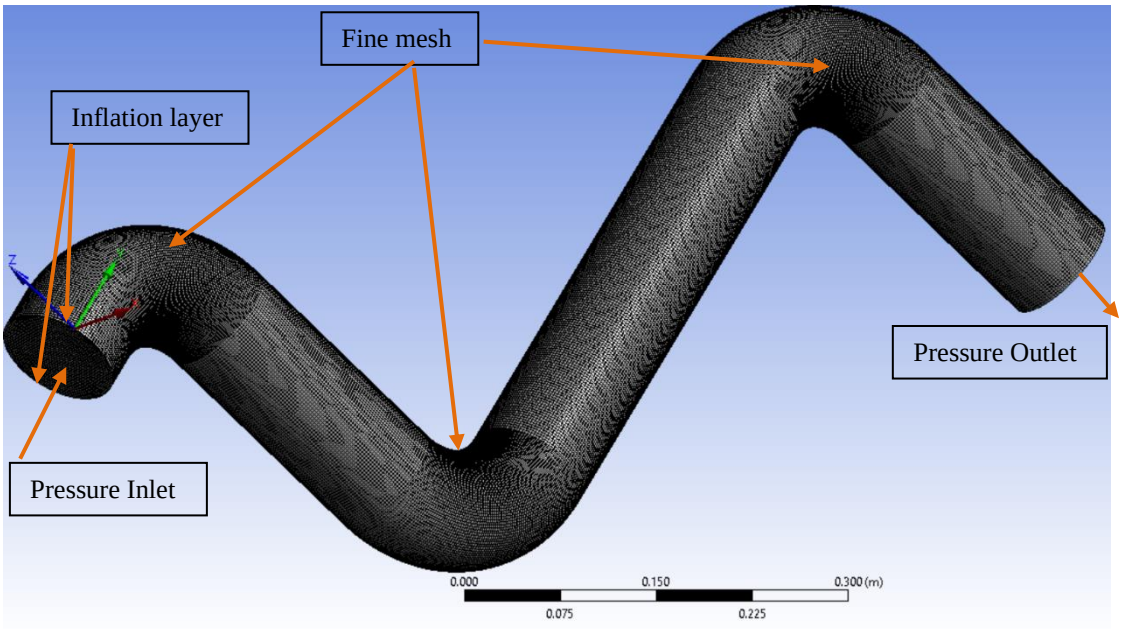

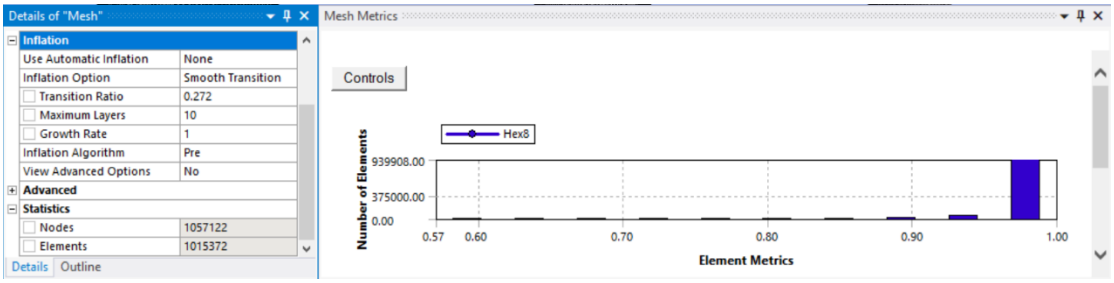


Figure 3.6: 3D Meshing using Fluent 21 and Orthogonal Quality

### 3.3.3 Calculation of sand injection velocity

The velocity was calculated from the mass flow rate of water obtained from mesh independent test which is equal to the sand injection velocity. The calculation details is shown in below.

$$\dot{m}_w = \rho_w \times A \times \vartheta \qquad \text{Equation 3.5}$$

Where,

$\dot{m}_w = mass\ flow\ rate\ of\ water$

$\rho_w = density\ of\ water$

$A = cross\ section\ area\ of\ pipe\ inlet$

$\vartheta = assumed\ velocity\ of\ sand\ particle$

### 3.3.4 Calculation of total mass flow rate of sand

Utilizing the mass flow rate of water from the mesh independent test and the sediment content of the tested sample, the total mass flow rate of sand was computed. The calculation details is shown below.

$$\dot{m}_s = \frac{\dot{m}_w}{\rho_w} \times PPM \times 10^{-3} \qquad \text{Equation 3.6}$$

Where,

$\dot{m}_s = total\ mass\ flow\ rate\ of\ sand$

$\dot{m}_w = mass\ flow\ rate\ of\ water$

$\rho_w = density\ of\ water$

$PPM = sediment\ concentration\ (parts\ per\ million)$

### 3.3.5 Numerical Modelling

This setting defines the viscous model, discrete phase model, sand particle injection, and boundary condition for erosion model analysis.

**Viscous Model (Turbulence model)**

The viscous model made use of the Realizable k-ε model in ANSYS Fluent. Strong streamline curvature, vortices, and rotation are among the flow characteristics that distinguish it from the standard k-ε model. A modified transport equation for the dissipation rate, ε, was obtained from an accurate equation for the transport of the mean-square vorticity fluctuation and is included in the model as an alternate formulation for the turbulent viscosity. When a model is said to be "realizable," it indicates that it complies with specific mathematical restrictions on the Reynolds stresses that are in line with the physics of turbulent flow. Additionally, Standard wall function was employed for investigation of Near-wall treatment.

**Erosion modelling**

Generic Fluent, Finnie, McLaury, and Oka are the four erosion models that make up ANSYS Fluent in general. Slurry flows have made the greatest use of the McLaury erosion model, which was developed to predict the rate at which solid particles erosion in water. On this study, the McLaury erosion model was preferred.

For erosion analysis in ANSYS Fluent, discrete phase model (DPM) was used for sand particle injection. Sand particle was used as inert particle type and with surface injection. Diameter distribution was taken as uniform with the value, 0.2 mm, that was obtained from PSD curve of sediment sample. The velocity magnitude was taken as 11 m/s which was obtained from mass flow rate from mesh independent test. Additionally, the sediment concentration of the sample was used to calculate the total mass flow rate of sand by using Equation 3.6. The maximum erosion rates were identified at different sediment concentration and then compared with the calculated erosion rate density from field measurement.

**Boundary conditions**

In ANSYS Fluent, the flow simulation was carried out. Drawing, field measurement, and ANSYS CFD analysis were used to collect all the required data. The findings so acquired were examined in the ANSYS Fluent post to observe the required erosion rate

density, pressure distribution, and velocity distribution. Table 3.1 below displays the details of parameters and boundary conditions utilized during the erosion simulation.

Table 3.1: Parameters and boundary conditions for erosion simulation

| | |
|---|---|
| Analysis type | Pressure based, Steady state |
| Fluid and Particle | Water and Sand |
| **Inlet/ Outlet condition** | |
| Gauge total pressure inlet/ outlet | 150000 Pa, 0 Pa |
| Direction | Normal to boundary |
| Turbulent intensity | 5% |
| Turbulent viscosity ratio | 10 |
| Particle motion | escape |
| **Wall condition** | |
| Wall motion | Stationary wall |
| Shear condition | No slip |
| Roughness | Standard |
| Particle motion | Reflect |
| **Erosion Analysis** | |
| Erosion model | McLaury erosion model |
| Average diameter of sand | 0.2mm |
| Viscous model | Realizable k-ε, standard wall function (Turbulence intensity = 5%) |
| Injection velocity of sand | 11 m/s |
| Injection type | Surface, inject using face normal direction |
| Mass flow rate of sand | Different for different ppm using equation 3.6 |
| Density of sand | 2650 kg/m3 |
| Wall material | Steel SS304 |
| Pressure-velocity coupling | SIMPLE method |
| Spatial discretization | Least square based, PRESTO |
| Number of iteration | 1000 |
| Convergence criterion | 0.001 residual |

Mineral content analysis of sand sample revealed that quartz comprised around 70% of weight of sample. So, density of sand was taken as density of quartz; 2650 kg/m$^3$

(Baidar et al., 2015). The material used on PBP of CHEPS is Austenitic SS304 having density 8030 kg/$m^3$. Table 3.2 shows the material composition of the PBP.

Table 3.2: Material composition of PBP

| Element | % Present |
|---|---|
| Carbon | 0.07 |
| Chromium | 17.50 to 19.50 |
| Manganese | 2.00 |
| Silicon | 1.00 |
| Phosphorous | 0.045 |
| Sulphur | 0.015 |
| Nickel | 8.00 to 10.50 |
| Nitrogen | 0.10 |
| Iron | Balance |

### 3.3.6 Result validation

The result obtained through the computational analysis and filed measurement was compared. The validation of the result was done by comparing the location of erosion prone area (from photograph) and erosion rate density at different locations.

## 3.4 Computational Study of proposed design

Sediment erosion and cavitation erosion are the two primary causes of erosion in pipelines and bends. In this study only sediment erosion analysis was done. Sediment erosion is caused by the sediment flow velocity impacting the wall components mainly in elbow when flow suddenly changes its direction. Variations in pressure have an additional influence on velocity. A sudden change in flow velocity and the fluid's kinetic energy combine to quickly create a pressure wave known as a pressure surge. In this instance, the chamber was built to replace the lower elbow on the assumption that by extending the transition period between changes in flow direction and surge pressure, sediment erosion on the surface of the wall would be partially mitigated.

### 3.4.1 3D Geometry creation

The 2D drawing was created in CATIA V5 and then it was transferred into 3D. Only the lower side elbow was changed with a chamber box in this instance, and the measurements are given in millimeters.

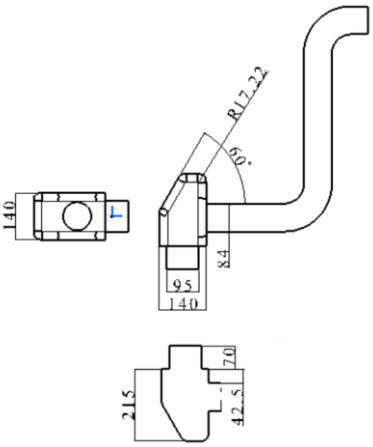


(a) 2D drawing

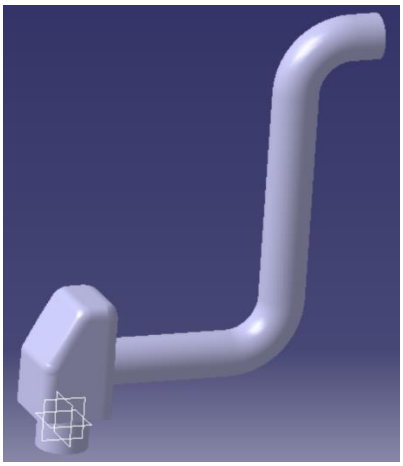

(b) 3D drawing

Figure 3.7: 2D and 3D CATIA drawing of proposed design (chamber)

### 3.4.2 Meshing

For mesh generation, the 3D geometry of an existing PBP was imported into ANSYS Fluent 21. The 3D domain as a whole was used to construct the mesh. To capture the impact of a sudden shift in flow direction, a fine mesh was utilized on the elbow with an O-grid tropology. Additionally, 6 inflation layers was utilized close to the wall to capture the effects of the viscous layer (boundary layer) on fluid flow.

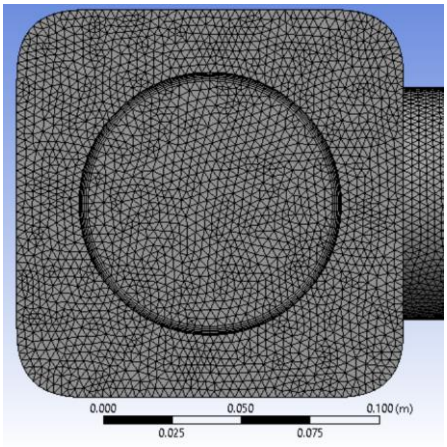


(a) Surface mesh

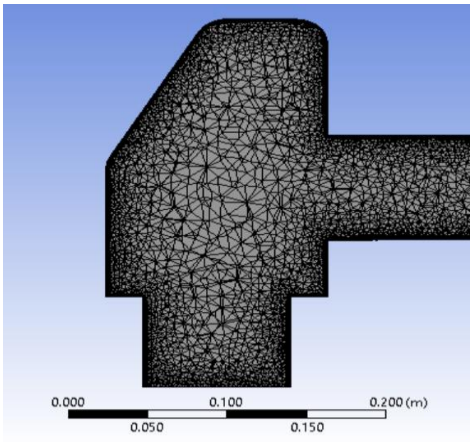


(b) Internal mesh

Figure 3.8: Mesh structure

### 3.4.3 Calculations

The water velocity determined by Equation 3.5 was considered to be equal to the sand injection velocity. Equation 3.6 was used to compute the total mass flow rate of sand. Furthermore, the boundary conditions applied were the same as in the previous case.

# CHAPTER FOUR: RESULTS AND DISCUSSION

## 4.1 Sediment Sample Results

The sediment sample was collected from Chameliya HPP's Draft Tube side and analyzed at Hydro Lab Pvt. Ltd. in Krishnal Galli, Lalitpur, Nepal. Following were the tests conducted:

### 4.1.1 Dry weight of suspended sediment sample

10 number of sediment samples were collected during the wet season (2021 May to August), when pipe failure due to erosion is most common, the concentration of sediment was measured. Each sample was collected in one liter of sediment led water, and the dry weight were measured after that sediment concentration was calculated (ppm). Figure 4.1 shows the concentration of sediment from 2021 May 3 to 2021 August 2. Sediment concentration was found rising from 420.20ppm (May 3) to 4262.30ppm (June 13) , then slightly decreasing to 4045.50ppm on June 23 and then rising again to a maximum of 5030.70 on July 4 and decreasing up to 2056.10ppm on August 2. The rise in concentration could be the result of high flood and construction activities (Hydropower construction, Road construction etc.). Over the course of the time, the average concentration was found to be 2718.39 ppm. The measured value of dry weight from lab is in APPENDIX A.

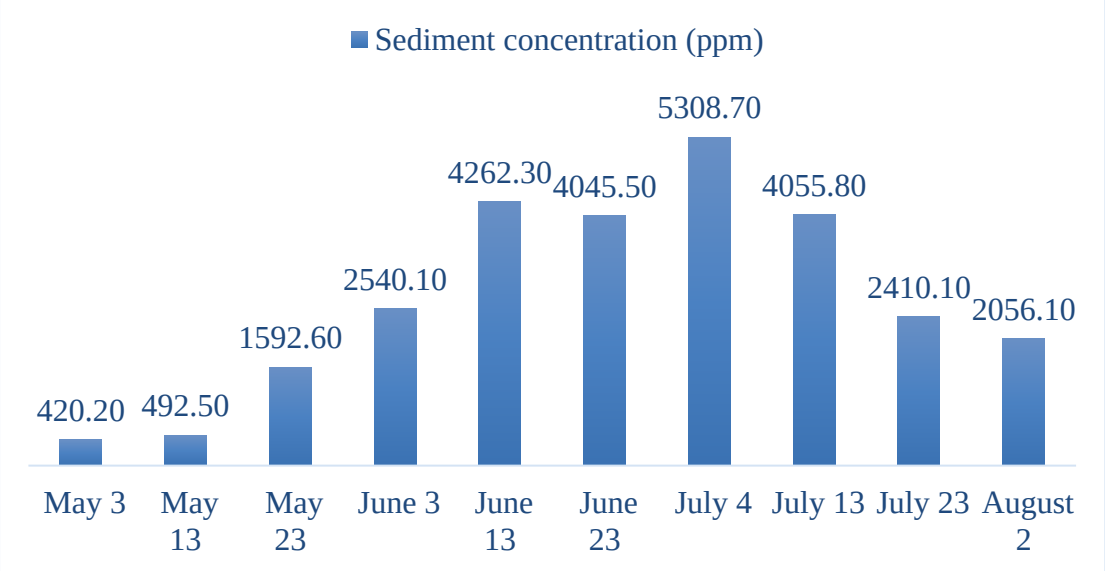


Figure 4.1: Concentration of sediment from 2021 May 3 to 2021August 2

### 4.1.2 Particle size distribution

Around 90% of the particles in BS 2078 Fagun (dry month) are under the range (0.01 to 0.1) mm whereas during same year of Shrawan (wet month) particle size are under the range (0.01 to 0.02) mm. However, the majority of the particles in the recent year BS 2079's rainy season (Jestha, Ashad, and Shrawan) were found to be in the range of (0.01 to 0.5) mm. Due to the flood rising in rainy season, particle size and sediment concentration may both rise. Human activities such as construction of a hydroelectric plant and the construction of roads in the upstream region may be responsible for larger particle size flowing this year compared to previous year. In this study, a quartz particle diameter of 0.2mm was used.

Figure 4.2 and Figure 4.3 show the PSD curve of BS 2078 & 2079 which is also in APPENDIX B.

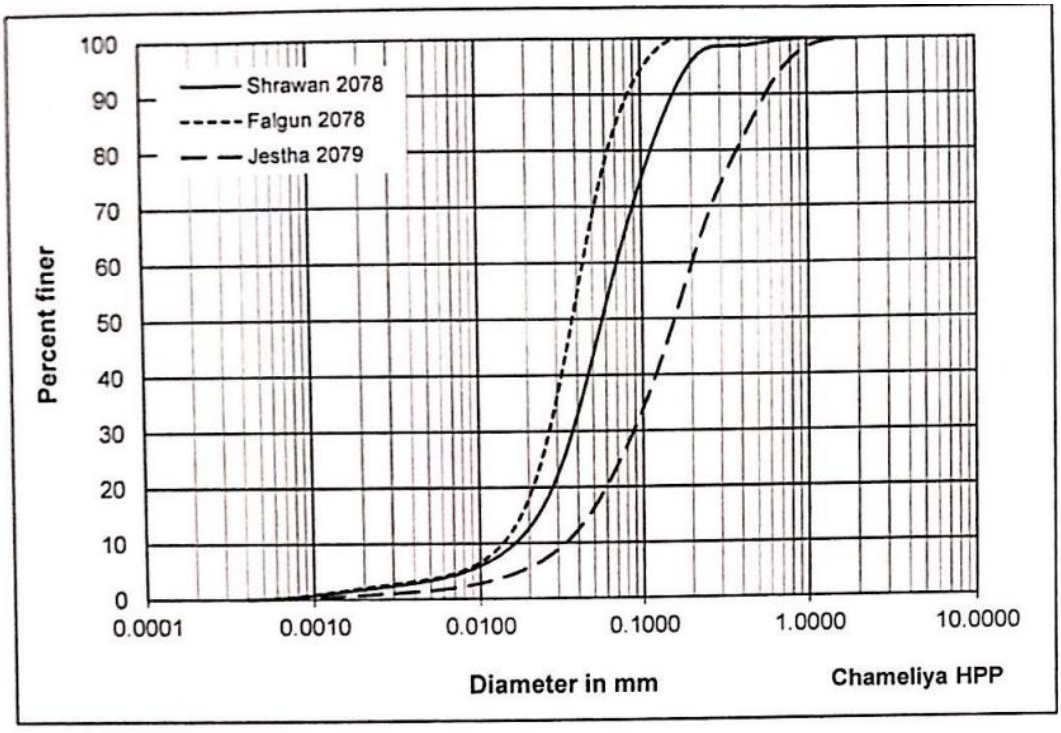


Figure 4.2: PSD graph of BS 2078 (Shrawan, Fagun) & 2079 Jeshtha

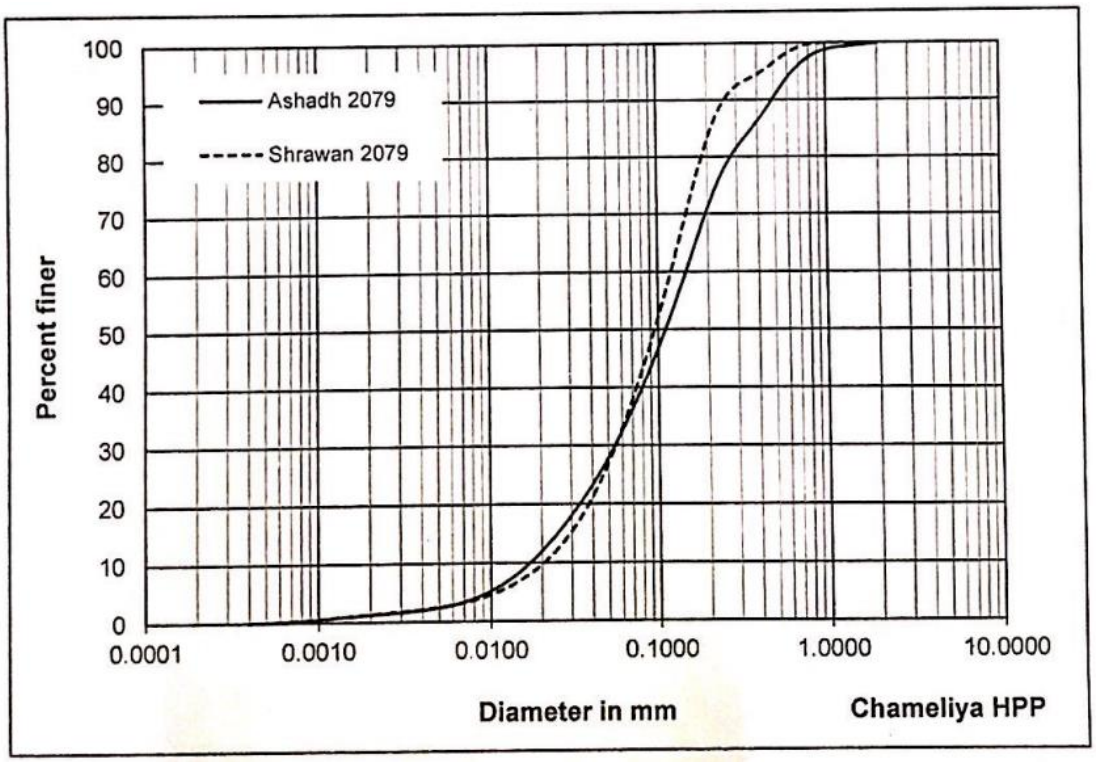


Figure 4.3: PSD graph of BS 2079 (Ashad & Shrawan)

### 4.1.3 Mineral content analysis

The mineral content analysis of the sediment sample collected from the Draft tube side of the Chameliya HPP is shown in Table 4.1 below. According to the analysis of the sediment sample, the sample contains quartz, feldspar, mica, tourmaline, garnet, hornblende, olivine, and clay. The most prevalent of them is quartz, which is present in around 67.6% of it. The mineral content is not at all variable, according to the sample analysis of different months. The major causes of elbow erosion are comprised of a total of around 70.8% of minerals (quartz, feldspar, tourmaline, garnet, hornblende, and olivine) that are harder than the elbow material.

Table 4.1: Mineral content analysis

| Minerals | | Average sample % | | | | | | Hardness (Moh's Scale) |
|---|---|---|---|---|---|---|---|---|
| | | BS 2078 Shrawan | BS 2078 Fagun | BS 2079 Jestha | BS 2079 Ashad | BS 2079 Shrawan | Average | |
| Quartz | | 67 | 66 | 69 | 68 | 68 | 67.6 | 7 |
| Feldspar | | 2 | 3 | 2 | 2 | 2 | 2.2 | 6 |
| Mica | | 15 | 14 | 13 | 13 | 13 | 13.6 | 2-3 |
| Other | A | 1 | 1 | 1 | 1 | 1 | 1 | ≥5 |
| | B | 15 | 16 | 15 | 16 | 16 | 15.6 | < 5 |

Other A: Tourmaline, Garnet, Hornblende and Olivine

Other B: Carbonate (14%), Clay, Organic matters, and upto 2% unidentified mineral and rock fragments (slate).

Detail analysis of the mineral content for the different months is in APPENDIX C.

## 4.2 Results of CFD simulation (Existing system)

### 4.2.1 Mesh independence

The mesh dependence test ensures that the best amount of meshes is selected without affecting output quality while making the best use of computational cost and time. Mesh independence test is conducted for several meshes utilizing physics defined mesh sizes of coarser (M1), coarse (M2), normal (M3), fine (M4), and finer mesh (M5) which is shown in Table 4.2.

Table 4.2: Mesh independent test

| Number of elements | Mass flow rate (kg/s) | Deviation from previous (%) |
|---|---|---|
| (M5) 3489500 | 75.12 | |
| (M4) 1644184 | 77.12 | 2.7% |
| (M3) 1015372 | 77.84 | 0.9% |
| (M2) 562500 | 89.53 | 15.0% |
| (M1) 277875 | 125.19 | 39.8% |

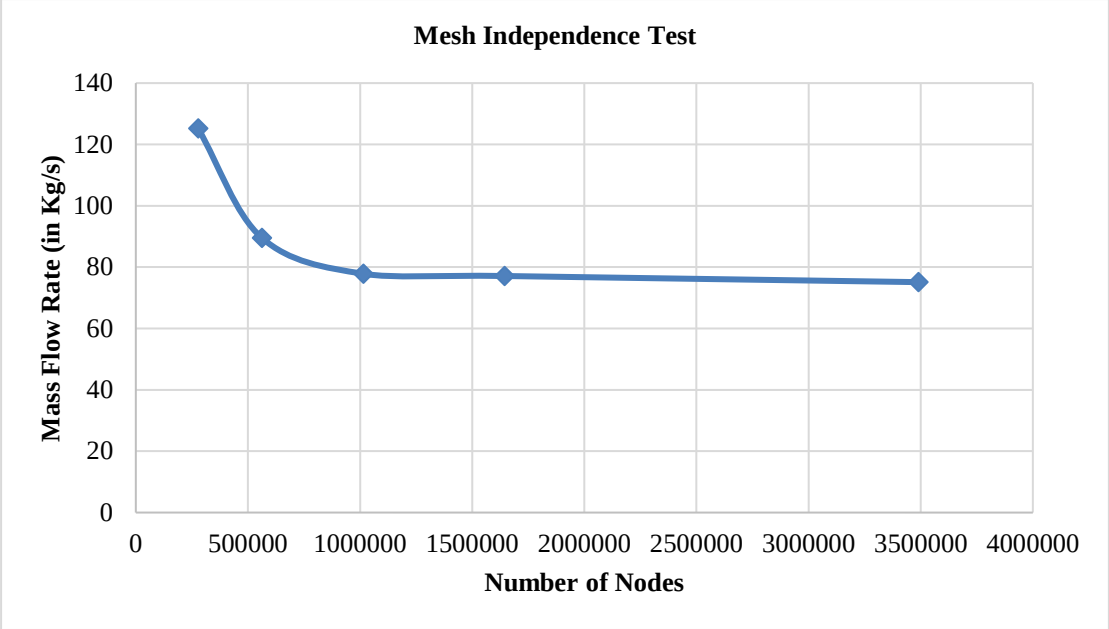


Figure 4.4: Mesh independence

The mesh independent test was performed by using the inlet, outlet pressure readings from field measurement (0.15Mpa, 0 MPa). Mesh size influences boundary layer refinement control in a direct proportion. The desired value (mass flow rate) varies from 277875 (M1) to 3489500 (M5) for the various element numbers, and mass flow rate was taken into consideration as the parameter of interest during the test. Figure 4.4's graph of the mesh independent test shows that the value of mass flow rate does not significantly change after a fine mesh of 1015372 (M3) elements. As a result, the M3 mesh set M3 (1015372 elements) was chosen from the mesh independence test to lower the computational cost and time taking into account the resources available. Further computational analysis of erosion rate also employed the equivalent mass flow rate value of 77.84 kg/s. The sand injection velocity was calculated by using the Equation 3.5 which was found to be 11m/s.

### 4.2.2 Pressure contour

Figure 4.5 represents the pressure distribution in PBP. From visualizing the figure, the pressure goes on decreasing almost smoothly along the center line of pipe moving from inlet to outlet but it is not as smooth along the wall surface where the pipe bends occur. Due to the sudden change in flow direction the pressure at bend extrados (outer curvature) was found higher than intrados (inner curvature). Here Zone 1 shows the

high pressure region and Zone 2 shows the low pressure region (even negative pressure region).

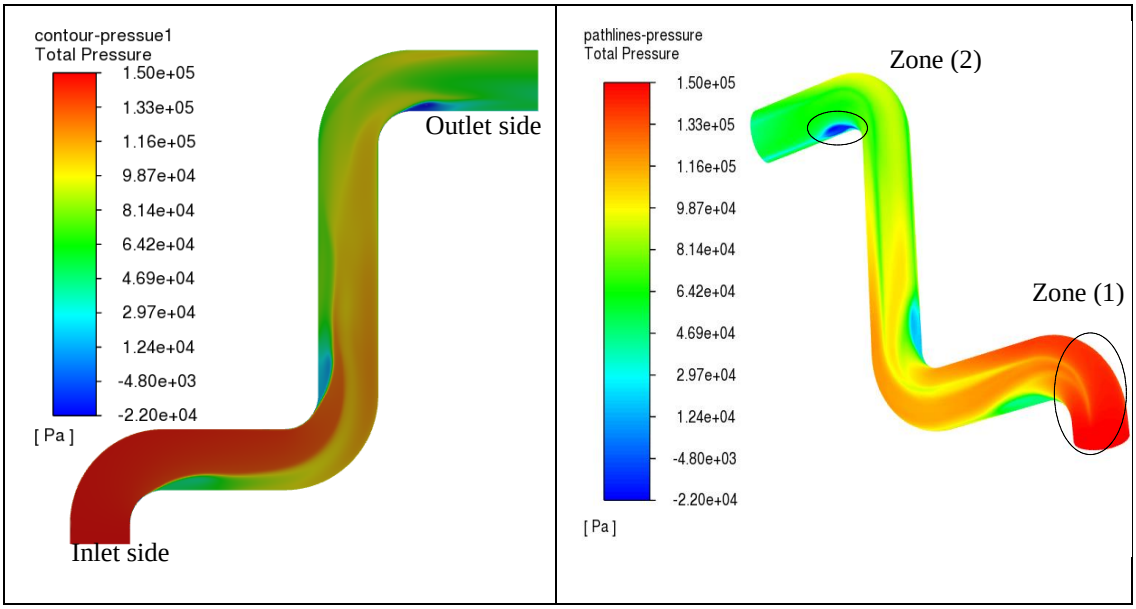


Figure 4.5: Pressure distribution in PBP

### 4.2.3 Velocity contour

The velocity distribution in the PBP is shown in Figure 4.6. With almost zero velocity occurred at the surface certain ahead of intrados (Zone 3) while moving from inlet to exit whereas the velocity at the bend intrados was found to be high.

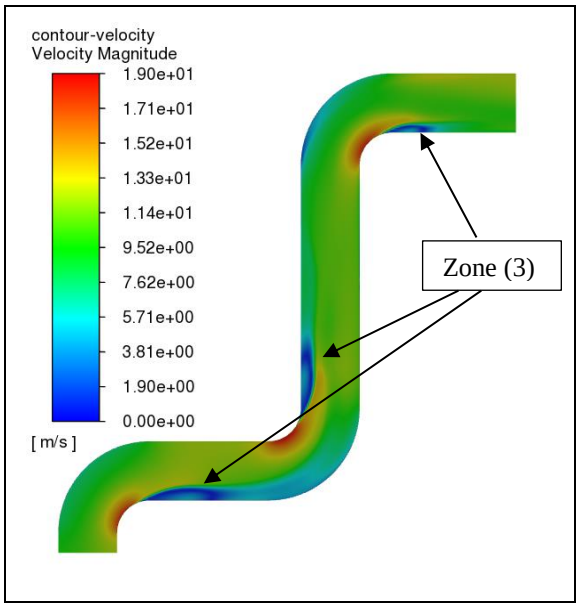


Figure 4.6: Velocity distribution in PBP

### 4.3 Field Investigation of Eroded Elbow

#### 4.3.1 Photographs

At the time of the field visit, the erosion in the PBP could be visually represented. The lower side elbow extrados area experienced excessive erosion. The Unit has repeatedly been shut down for the repair (repair by welding) of the leaking region because of the excessive erosion, mostly during the rainy season. Figure 4.7 shows the leakage occurring due to excessive erosion on elbow extrados.


Figure 4.7: Leakage due to excessive erosion on elbow

Elbow that was dismantled during overhauling period was cut into different sections and visualized and measured the thickness. Observing the erosion pattern as shown in Figure 4.8(b), the rate of erosion rises as one moves from the inlet (the bottom part) to the outlet (the upper portion). The outer curvature of the bend was found to have excessive erosion, holes, but the inner curvature had less erosion than the outer curvature which is shown in Figure 4.8(a).


(a) Excessive erosion area


(b) Erosion pattern

( c)Thickness measurement

Figure 4.8: Erosion pattern in internal surface of elbow and thickness measurement

### 4.3.2 Thickness measurement at different positions

The Vernier caliper having least count 0.02 mm was employed to measure the elbow's thickness (elbow embedded with headcover). The thickness was measured in different sections; side wall section (A, A', B, B', C, C', D, D', E, E',F, F', G, G', H, H', I, I') and Outer curvature section (1', 2', 3', 4', 5', 6', 7', 8', 9'), total 27 sections, in order to compute the loss of thickness due to erosion. The loss of thickness was calculated by subtracting the measured thickness from design thickness (10 mm). Figure 4.9 shows the positions of measurement and Figure 4.8(c) shows the thickness measurement.

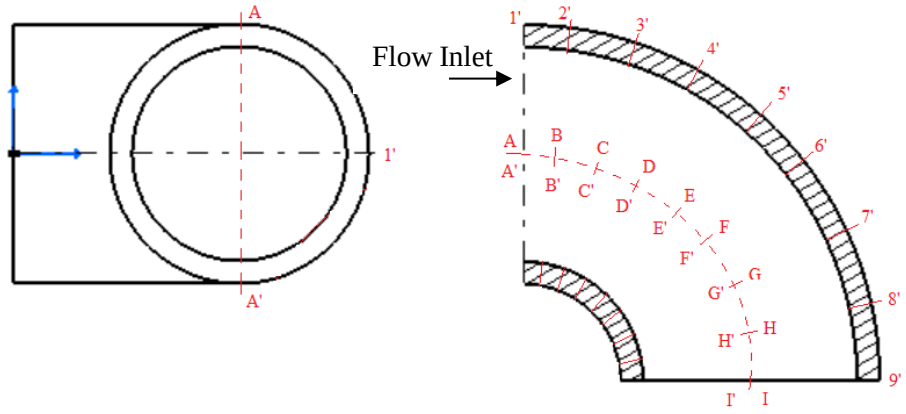


Figure 4.9: Different positions for thickness measurement

Table 4.3 shows the loss of thickness data that were calculated using Equation 3.2 and percentage of uncertainty error during thickness measurement were calculated by using Equation 3.1. The average loss of thickness and uncertainty error was found to be 5.54mm and 0.76% respectively.

Table 4.3: Loss of thickness at different location

| Position | Measured thickness (mm) | Loss in thickness (mm) | Uncertainty Error % |
|---|---|---|---|
| 1' | 9.08 | 0.92 | 0.22% |
| 2' | 8.16 | 1.84 | 0.25% |
| 3' | 7.04 | 2.96 | 0.28% |
| 4' | 4.50 | 5.50 | 0.44% |
| 5' | 2.20 | 7.80 | 0.91% |
| 6' | 2.50 | 7.50 | 0.80% |

| | | | |
|---|---|---|---|
| 7' | 1.60 | 8.40 | 1.25% |
| 8' | 1.70 | 8.30 | 1.18% |
| 9' | 1.50 | 8.50 | 1.33% |
| A | 9.04 | 0.96 | 0.22% |
| B | 8.54 | 1.46 | 0.23% |
| C | 7.04 | 2.96 | 0.28% |
| D | 6.50 | 3.50 | 0.31% |
| E | 3.56 | 6.44 | 0.56% |
| F | 3.02 | 6.98 | 0.66% |
| G | 1.26 | 8.74 | 1.59% |
| H | 1.20 | 8.80 | 1.67% |
| I | 1.80 | 8.20 | 1.11% |
| A' | 9.08 | 0.92 | 0.22% |
| B' | 9.14 | 0.86 | 0.22% |
| C' | 6.50 | 3.50 | 0.31% |
| D' | 5.80 | 4.20 | 0.34% |
| E' | 4.08 | 5.92 | 0.49% |
| F' | 1.40 | 8.60 | 1.43% |
| G' | 1.42 | 8.58 | 1.41% |
| H' | 1.36 | 8.64 | 1.47% |
| I' | 1.50 | 8.50 | 1.33% |
| Average | 4.46 | 5.54 | 0.76% |

### 4.3.3 Erosion rate density calculation

Erosion rate density at different locations (as shown in Figure 4.9) were calculated by using the Equation 3.4. For the purpose of calculating erosion rate density, the total erosion time (T) was assumed to be 3 months. Table 4.4 shows the erosion rate density at different location of thickness measurement. The locations 5', 6', 7', 8', 9', F, G, H, I, F', G', H' and I' were found to be the most eroded places, while the average erosion rate density was determined to be 5.71714E-06 kg/$m^2$s.

Table 4.4: Erosion rate density at different locations

| Position | Erosion rate density ($kg/m^2s$) |
|---|---|
| 1' | 9.50051E-07 |
| 2' | 1.90010E-06 |
| 3' | 3.05669E-06 |
| 4' | 5.67966E-06 |
| 5' | 8.05478E-06 |
| 6' | 7.74498E-06 |
| 7' | 8.67438E-06 |
| 8' | 8.57112E-06 |
| 9' | 8.77765E-06 |
| A | 9.91358E-07 |
| B | 1.50769E-06 |
| C | 3.05669E-06 |
| D | 3.61433E-06 |
| E | 6.65036E-06 |
| F | 7.20800E-06 |
| G | 9.02549E-06 |
| H | 9.08745E-06 |
| I | 8.46785E-06 |
| A' | 9.50051E-07 |
| B' | 8.88092E-07 |
| C' | 3.61433E-06 |
| D' | 4.33719E-06 |
| E' | 6.11337E-06 |
| F' | 8.88092E-06 |
| G' | 8.86026E-06 |
| H' | 8.92222E-06 |
| I' | 8.77765E-06 |
| Average | 5.71714E-06 |

### 4.4 CFD modeling of Erosion

Sand mass flow rates during the wet season were calculated by using the Equation 3.6, and the resulting data were utilized to compute erosion rate density. Table 4.5 shows the mass flow rate of sand that corresponds to the sediment concentration during the wet season. The average mass flow rate of sand corresponding to the average sediment concentration (2718.39 ppm) was found to be 0.2120 kg/s. The average mas flow rate was used to compute the erosion rate density at different locations (as shown in Figure 4.9).

Table 4.5: Mass flow rate of sand with different sediment concentration

| Date | Mass flow rate of water (kg/s) | Density of water ($kg/m^3$) | Sediment concentration (ppm) | Mass flow rate of sand (kg/s) |
|---|---|---|---|---|
| May 3 | 77.84 | 998.20 | 420.20 | 0.0328 |
| May 13 | 77.84 | 998.20 | 492.50 | 0.0384 |
| May 23 | 77.84 | 998.20 | 1592.60 | 0.1242 |
| June 3 | 77.84 | 998.20 | 2540.10 | 0.1981 |
| June 13 | 77.84 | 998.20 | 4262.30 | 0.3324 |
| June 23 | 77.84 | 998.20 | 4045.50 | 0.3155 |
| July 4 | 77.84 | 998.20 | 5308.70 | 0.4140 |
| July 13 | 77.84 | 998.20 | 4055.80 | 0.3163 |
| July 23 | 77.84 | 998.20 | 2410.10 | 0.1879 |
| August 2 | 77.84 | 998.20 | 2056.10 | 0.1603 |
| Average | 77.84 | 998.20 | 2718.39 | 0.2120 |

#### 4.4.1 Erosion prone area

Figure 4.10 shows the several locations where the PBP wall has experienced erosion. The average sediment concentration during the wet season was used to calculate the erosion rate density in ANSYS Fluent 21, McLaury model of erosion. The elbows' outside curvature (a, b, and c) was found to be more risk to erosion than other areas. Among the three elbows, the lower side elbow area (a) was found as the erosion prone area. So, the field measurement was done mainly on the lower side elbow.

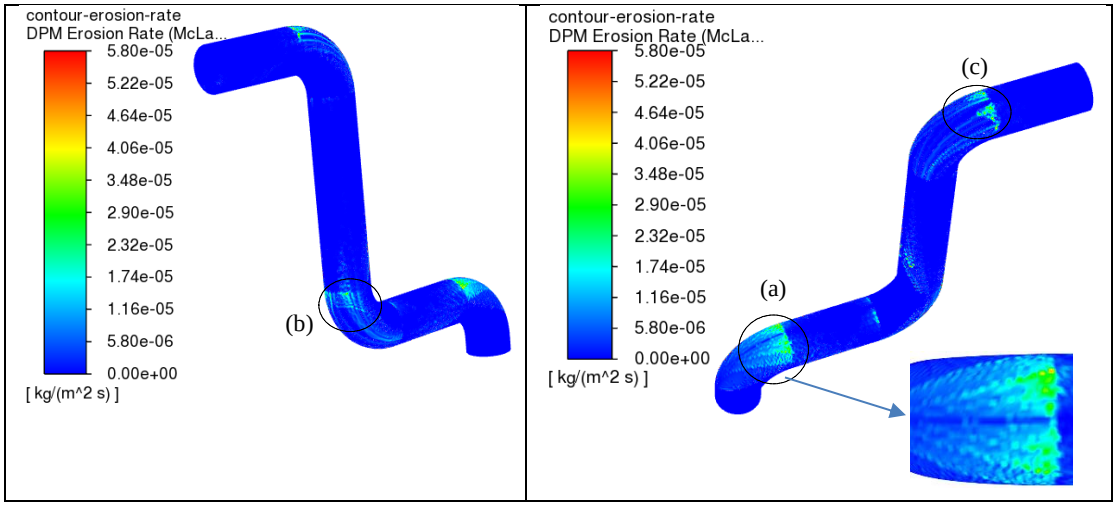


Figure 4.10: Erosion rate density contour

### 4.4.2 Erosion at different sediment concentration

Samples taken during the wet season (2021 May to August), when pipe failure due to erosion has been most common, the concentration of sediment was measured from Hydro Lab Pvt. Ltd, Lalitpur. The different measured values of sediment concentration were used to observe the erosion rate density.

According to Figure 4.11, erosion rate rises in response to rising sediment concentrations and vice versa. The leakage from the balance pipe caused by sediment erosion will thus probably happen more frequently during the rainy season when sediment flow is at its highest. It would be concluded that, Sediment concentration is one of the primary factors causing erosion on material surfaces. The sediment concentration and corresponding erosion rate density value are presented in tabular form in APPENDIX D.

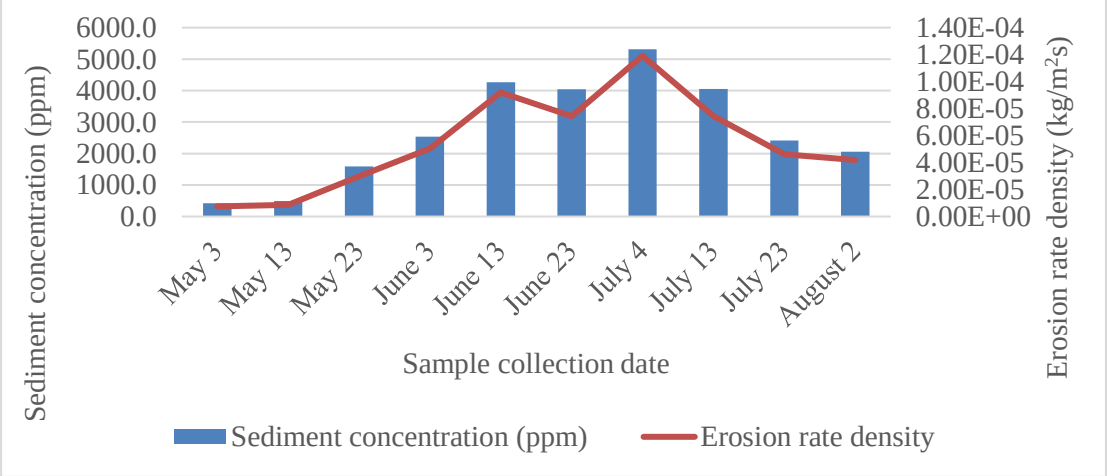


Figure 4.11: Erosion rate density at different Sediment concentration

### 4.4.3 Erosion rate density at different locations

Erosion rate density at different locations (as shown in Figure 4.9) were also computed from simulation by using average sediment concentration of wet season (2718.39 ppm). Table 4.6 shows the computed values of erosion rate density at different location of thickness measurement. The locations 6', 7', 8', 9', F, G, H, I, F', G', H' and I' were found to be the most eroded places, while the average erosion rate density was determined to be 1.01199E-05kg/$m^2$s.

Table 4.6: Erosion rate density at different locations

| Position | Erosion rate density from simulation (kg/$m^2$s) |
|---|---|
| 1' | 1.00346E-06 |
| 2' | 1.05794E-06 |
| 3' | 2.09893E-06 |
| 4' | 8.16256E-06 |
| 5' | 9.18934E-06 |
| 6' | 1.01555E-05 |
| 7' | 1.51256E-05 |
| 8' | 2.57234E-05 |
| 9' | 2.58971E-05 |
| A | 1.22125E-06 |
| B | 1.26374E-06 |
| C | 2.13137E-06 |
| D | 1.03283E-06 |
| E | 6.91243E-06 |
| F | 1.12359E-05 |
| G | 2.01434E-05 |
| H | 2.12276E-05 |
| I | 2.13577E-05 |
| A' | 1.24729E-06 |
| B' | 1.27376E-06 |
| C' | 2.02142E-06 |
| D' | 2.05223E-06 |
| E' | 6.93564E-06 |

| | |
|---|---|
| F' | 1.12416E-05 |
| G' | 2.04302E-05 |
| H' | 2.13527E-05 |
| I' | 2.17433E-05 |
| Average | 1.01199E-05 |

### 4.5 Comparison of Results

In the following two methods, the results of computational and experimental study were compared.

#### 4.5.1 Qualitative comparison

In the qualitative comparison, the erosion-prone area was identified by photographing the running elbow and the disassembled deteriorated elbow during the overhauling period. The erosion at the extrados of the lower side elbow was found to be excessive due to the high pressure and direct impact on the surface, as illustrated in Figure 4.7 and Figure 4.8. The results from simulation also indicated that the erosion-prone region was found at the extrados of lower side elbow, as illustrated in Figure 4.10. In comparison, According to simulation and experiment results, the position of the erosion-prone area was found to be identical.

#### 4.5.2 Quantitative comparison

The erosion rate density calculated from field measurement using 3 months (wet season) of erosion running time and loss of wall thickness and was compared with the value of erosion rate density from ANSYS Fluent simulation using average sediment concentration of 3 months (wet season). Following Figures show the comparison of simulation and experiment results on different locations (outer radius of curvature; 1’ to 9’, front side wall; A to I, and backside wall; A’ to I’) of elbow.

**i. Outer curvature surface of elbow**

In comparison with experiment value, the simulation value of erosion rate density was found to be;

(i) Follow the same way as the experimental value.

(ii) Somewhat lower at positions 2' and 3' but higher than the experimental value overall.

(iii) Deviation increases from position 7' to position 9'.

(iv) Maximum value of erosion rate density was found to be in same position 9' from both simulation and experiment.

(v) The deviation in average was found to be 71.08%.

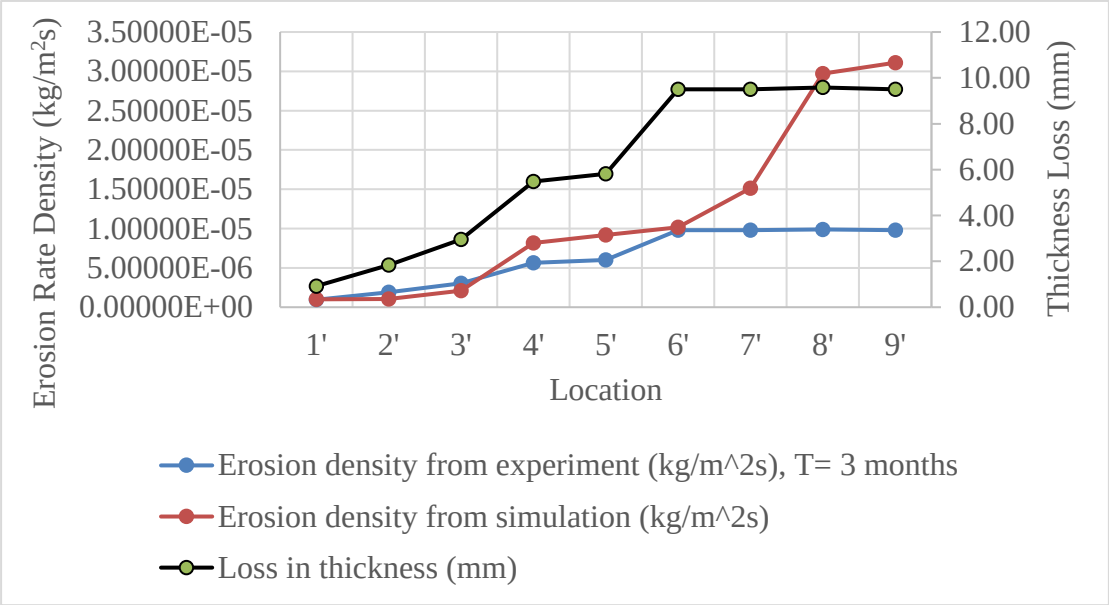


Figure 4.12: Comparison graph of erosion rate density at outside curvature

The comparison with values of Erosion rate density is presented in tabular form in APPENDIX G.

### ii. Front side wall of elbow

In comparison with experiment value, the simulation value of erosion rate density was found to be;

(i) Follow the same way as the experimental value.

(ii) Somewhat lower at positions B, C and D but higher than the experimental value overall.

(iii) Deviation rises from position G to I.

(iv) The erosion prone location was found to be in position H from experiment and in position I from simulation.

(v) The deviation in average was found to be 74.42%.

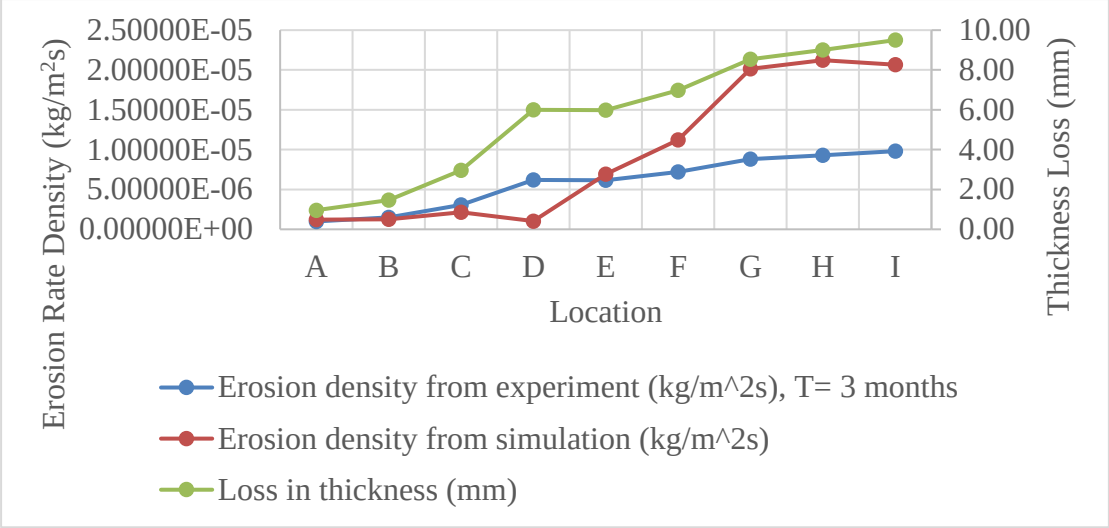


Figure 4.13: Comparison graph of erosion rate density at front side wall

The comparison with values of Erosion rate density is presented in tabular form in APPENDIX G.

### iii. Back side wall of elbow

In comparison with experiment value, the simulation value of erosion rate density was found to be;

(i) Follow the same way as the experimental value.

(ii) Somewhat lower at positions C' & D' but higher than the experimental value overall.

(iii) Deviation increases from position G' to I'.

(iv) The maximum value of erosion rate density was found to be in same position I' from both simulation and experiment.

(v) The deviation in average was found to be 69.90%.

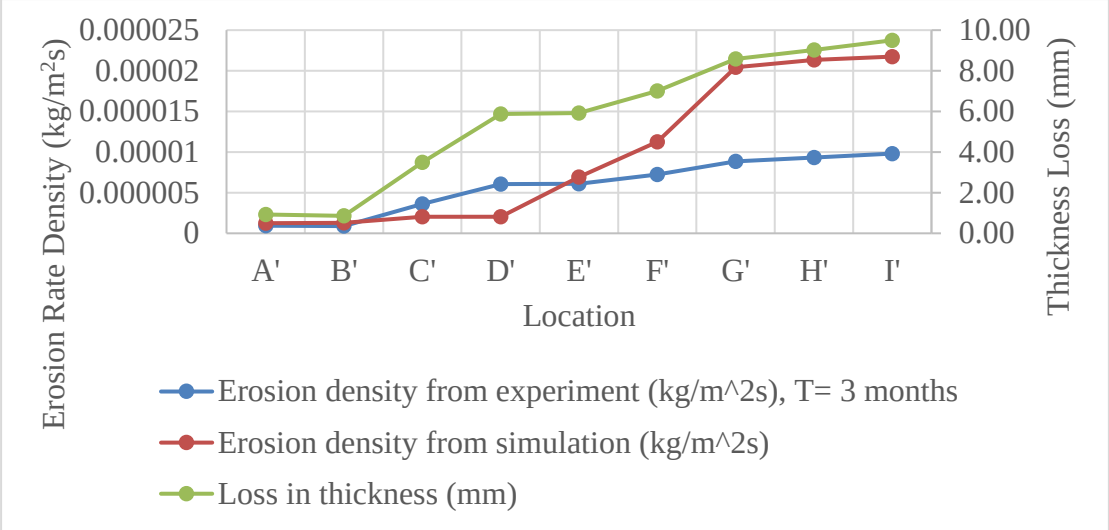


Figure 4.14: Comparison graph of erosion rate density at back side wall

The comparison with values of Erosion rate density is presented in tabular form in APPENDIX G.

It was discovered from all three comparisons (Figure 4.12, Figure 4.13 and Figure 4.14) that the erosion rate rises when moving from inlet to exit, albeit marginally decreasing in a few spots. The zone of outer curvature (4' to 9') and both side walls (E E' to I I') were found to be erosion prone area which is also shown in Figure 4.15. In addition, erosion rate density obtained from simulation exhibits the same pattern as the actual value, with an average difference of 69.58 percent. This discrepancy may have been brought about by measurement-related instrumentation errors, discretization mistakes connected to the numerical technique for solving equations, and flow-normalization assumptions made during numerical modeling.

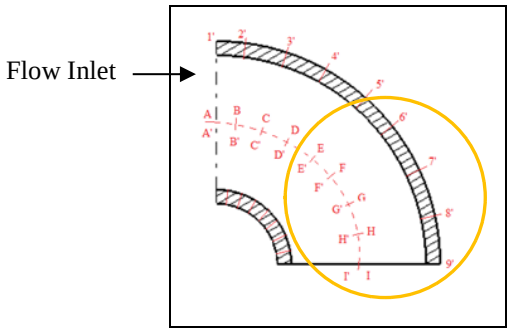


Figure 4.15: Location of erosion prone area

### 4.6 Results of CFD simulation (Proposed design)

#### 4.6.1 Mesh independence

Table 4.7: Mesh independent test

| Number of elements | Mass flow rate (kg/s) | Deviation from previous (%) |
|---|---|---|
| (M6) 7196499 | 48.57 | |
| (M5)2494459 | 49.49 | 1.9% |
| (M4) 1332927 | 49.96 | 0.9% |
| (M3) 721791 | 54.05 | 8.2% |
| (M2) 297997 | 59.76 | 10.6% |
| (M1) 82571 | 69.89 | 17.0% |

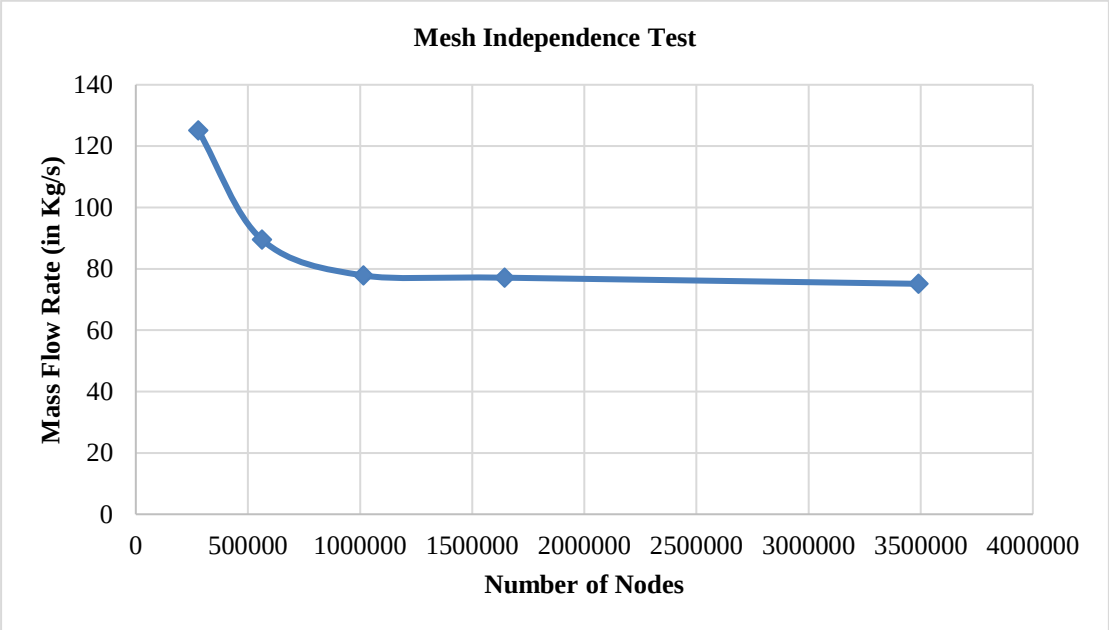


Figure 4.16: Mesh independence

The mesh independent test was performed by using the inlet, outlet pressure readings from field measurement (0.15Mpa, 0 MPa). Mass flow rate was taken into consideration as the parameter of interest during the test. Figure 4.16's graph of the mesh independent test shows that the value of mass flow rate does not significantly change after a fine mesh of 1332927 (M4) elements. As a result, the M4 elements was chosen from the mesh independence test. Further computational analysis of erosion rate also employed the equivalent mass flow rate value of 49.96 kg/s. Sand injection velocity was calculated by using the Equation 3.5 and found to be 7.06m/s.

### 4.6.2 Pressure contour & Velocity contour

According to pressure contours, pressure was high throughout the chamber box, sudden decreased across a very small surface area (the connection between the chamber and pipe), and then gradually decreased at the outflow.

According to the visualization of velocity contours, flow was discovered to be accelerated close to the joint of the chamber and pipe, while velocity becomes noticeably low at the chamber head's perimeter. It was discovered that the outlet velocity was higher than the inlet velocity, indicating that the flow would exit through the balancing pipe.

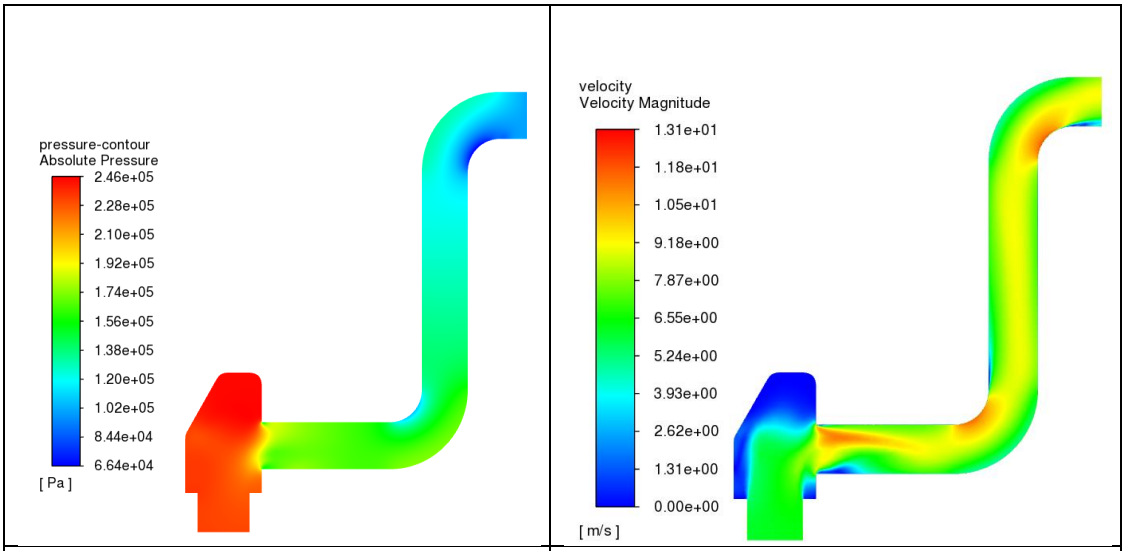


(a) Pressure contours (b) Velocity contours

Figure 4.17: Pressure and velocity contours

### 4.6.3 Results comparison with Existing system

Simulation Results of Existing and Proposed design were compared on the following basis.

#### i. Comparison of erosion rate density

Comparison of erosion rate density between the two PBP systems (existing and proposed) is shown Figure 4.18. With the exception of 492.50ppm, the maximum erosion rate density for various sediment concentrations obtained for the proposed design was determined to be lower than that of the existing PBP system. In comparison to the existing system, the proposed design showed an average 13.49% reduction in erosion rate density.

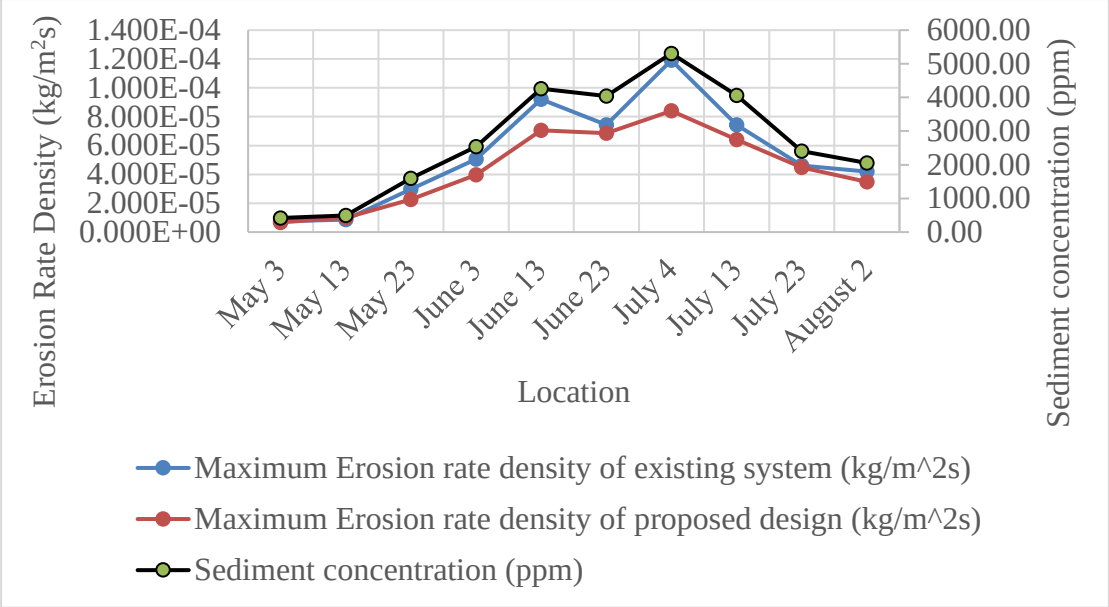


Figure 4.18: Comparison of erosion rate density

According to the simulation results, both the existing system and the proposed design exhibit rising erosion rate density with increasing sediment concentration and vice versa. However, it was found that for all sediment concentrations, with the exception of (May 13, 492.50ppm), the erosion rate density of the proposed case was lower than that of the existing system, which may be related to the stochastic/ unpredictable characteristics of particle flow. For the highest value of sediment concentration (July 4, 5308.70ppm), erosion rate density for proposed system was found to be 29.45% lower than that of existing system. Details comparison is presented in tabular form in APPENDIX H.

### ii. Comparison of erosion pattern

The simulation findings for each of our study's cases clearly demonstrate that erosion-prone locations were discovered to be relocated away from the chamber. There were a few little erosion sites evident close to the pipe and chamber intersection. Larger regions with substantial erosion rate density values were seen close to the downstream bend extrados of two elbows. Figure 4.19 shows the erosion patterns for the proposed (left) and existing (right) systems of PBP for various concentrations (ppm) of sediment.

**1. For 492.50ppm**

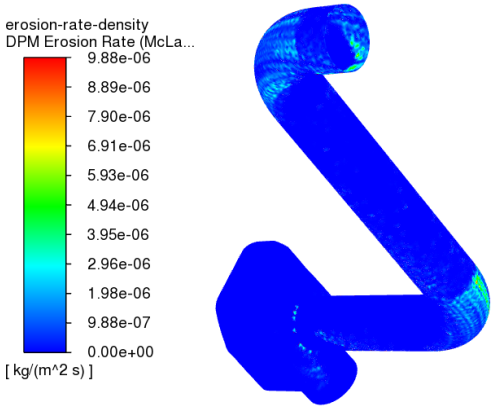


(a) ERD: 9.87567E-06 kg/m$^2$s

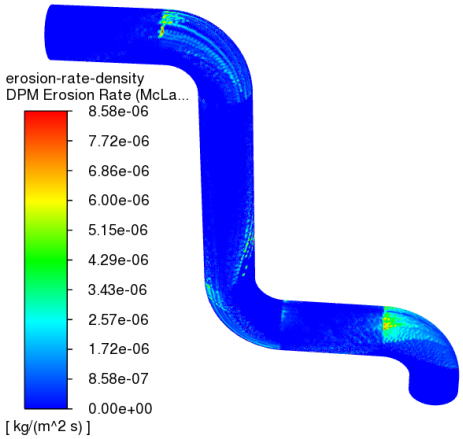


(a') ERD: 8.57670E-06 kg/m$^2$s

**2. For 1592.60ppm**

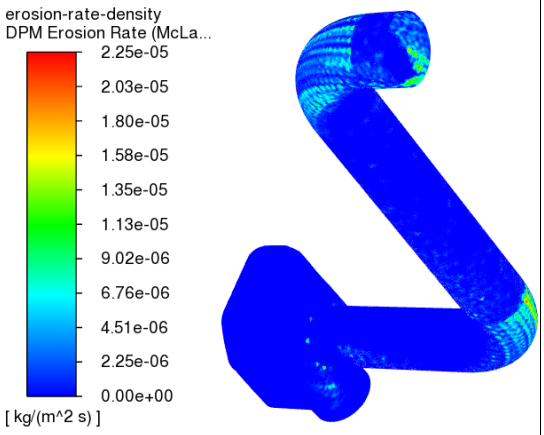


(b) ERD: 2.25411E-05 kg/m$^2$s

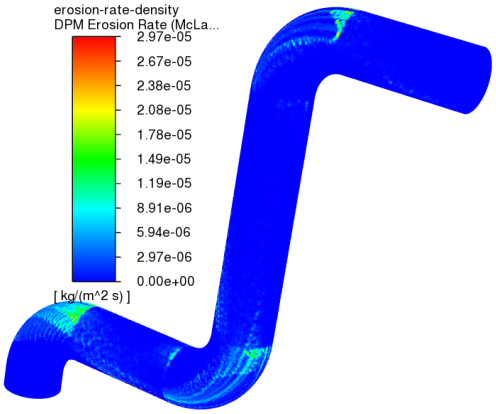


(b') ERD: 2.97017E-05 kg/m$^2$s

**3. For 2540.10ppm**

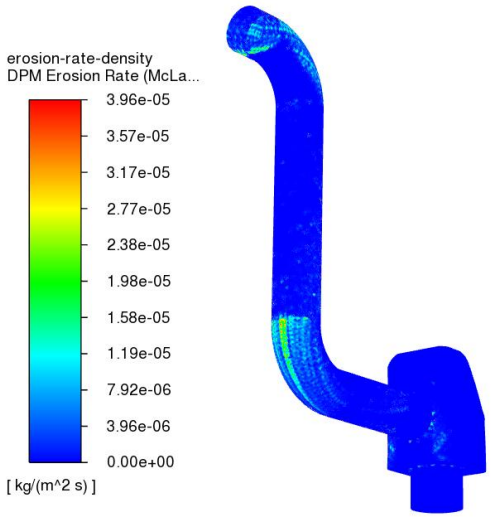


(c) ERD: 3.96211E-05 kg/m$^2$s

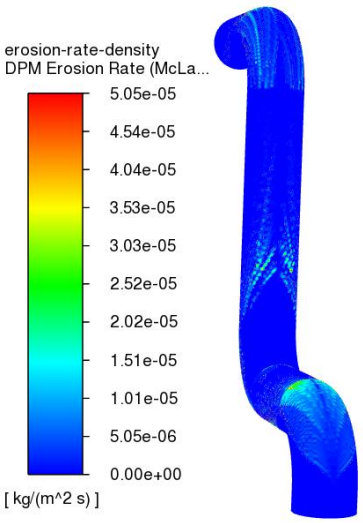


(c') ERD: 5.04865E-05 kg/m$^2$s

**4. For 4262.30ppm**

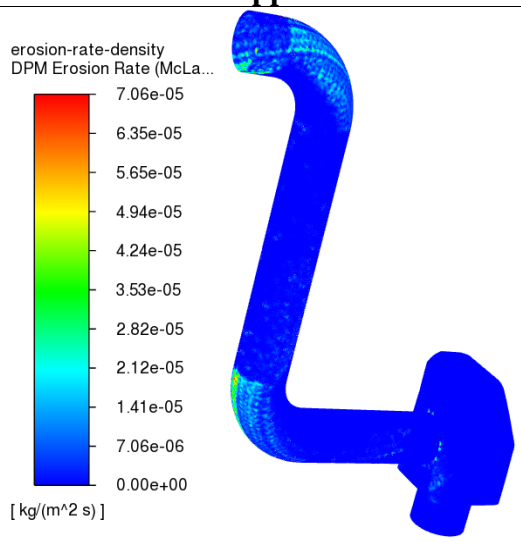


(d) ERD: 7.06060E-05 kg/m$^2$s

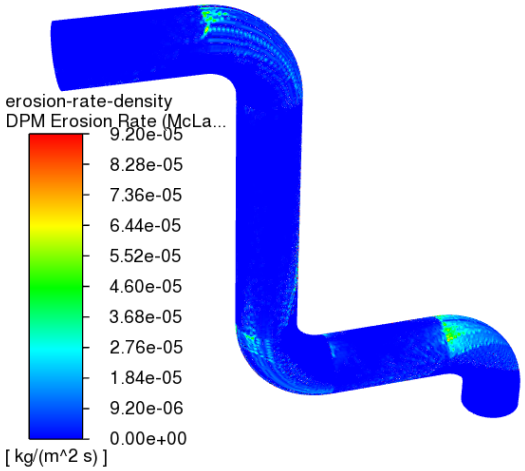


(d') ERD: 9.19843E-05 kg/m$^2$s

**5. For 4045.50ppm**

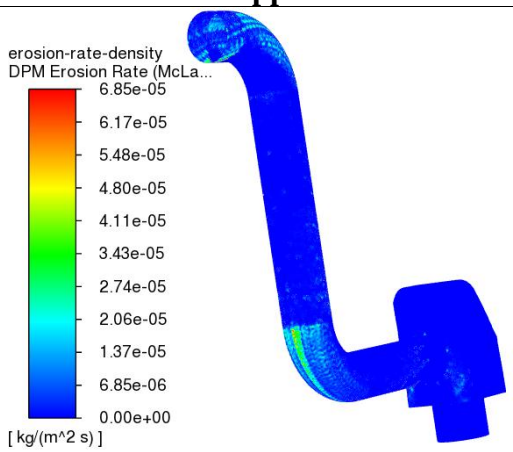


(e) ERD: 6.85409E-05 kg/m$^2$s

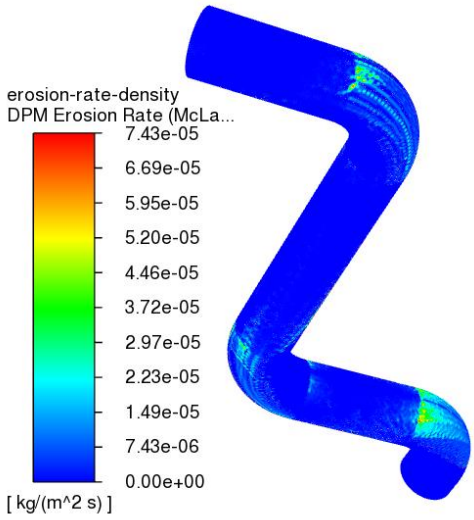


(e') ERD: 7.43161E-05 kg/m$^2$s

**6. For 5308.70ppm**

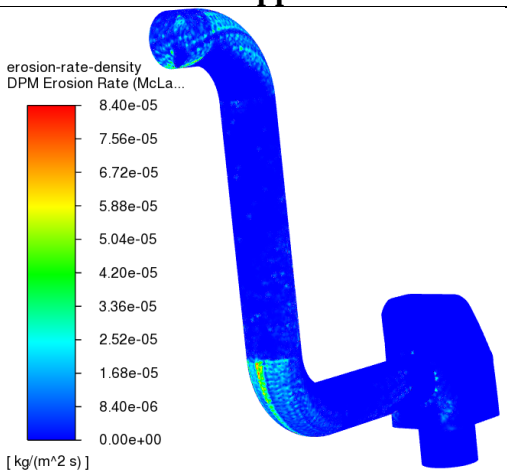


(f) ERD: 8.40158E-05 kg/m$^2$s

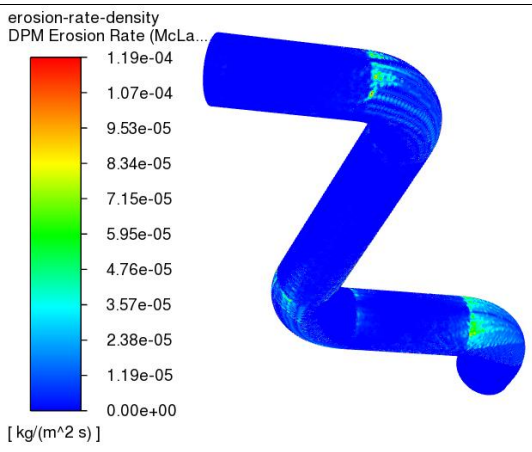


(f') ERD: 1.19090E-04 kg/m$^2$s

**7. For 4055.80ppm**

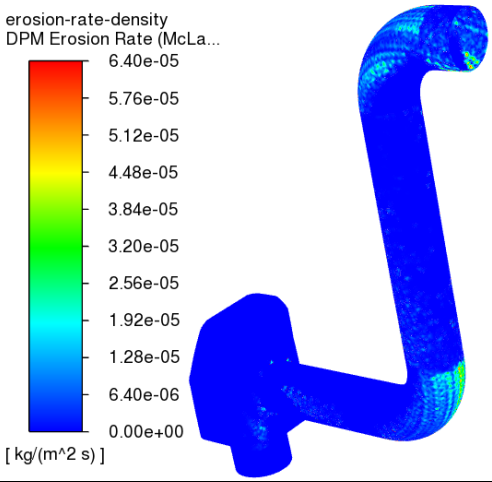


(g) ERD: 6.40305E-05 kg/m$^2$s

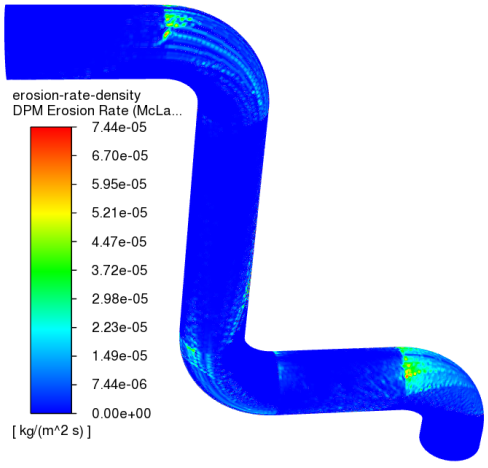


(g') ERD: 7.44253E-05 kg/m$^2$s

**8. For 2410.10ppm**

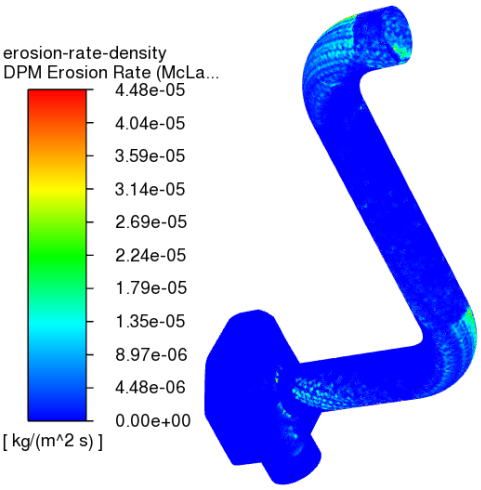


(h) ERD: 4.48428E-05 kg/m$^2$s

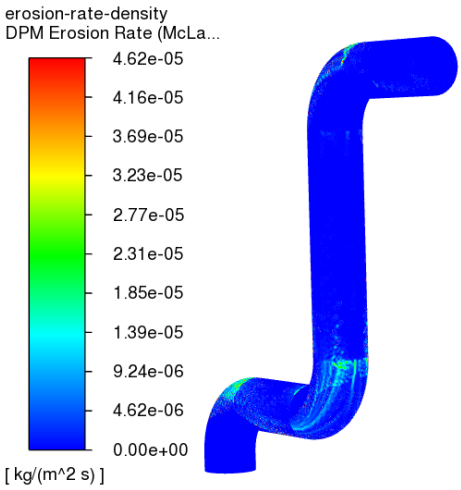


(h') ERD: 4.61854E-05 kg/m$^2$s

**9. For 2056.10ppm**

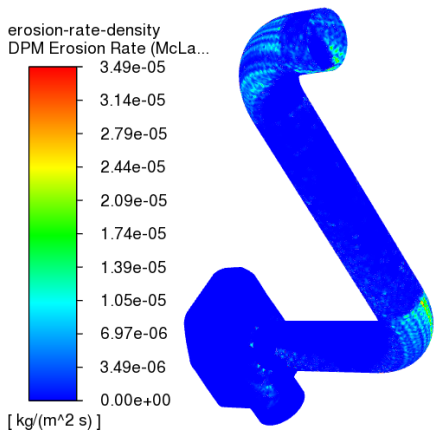


(i) ERD: 3.48653E-05 kg/m$^2$s

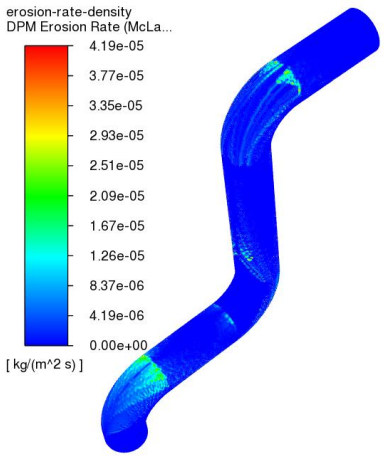


(i') ERD: 4.18667E-05 kg/m$^2$s

Figure 4.19: Comparison of erosion pattern

It was found that maximum erosion rate density for various sediment concentrations obtained for the proposed design was determined to be lower than that of the existing PBP system. In comparison to the existing system, the proposed design showed an average 13.49% reduction in erosion rate density. Erosion-prone locations were discovered to be relocated away from the chamber. There were a few little erosion sites evident close to the pipe and chamber intersection. Larger regions with substantial erosion rate density values were seen close to the downstream bend extrados of two elbows. This modification has reduced the erosion rate density which is expected to increase the system life a bit further. In addition, the shift of erosion prone area, makes the pipe and elbows with flange connection to erode. This location is much easier to replace in case the erosion occurs and pipe starts to leak. In case of erosion of the lower elbow (elbow embedded with headcover), it takes about 60 to 70 hours of shutdown to repair the elbow as it is inside the head cover which is due to dismantling of turbine guide bearing and linkage of gate operating ring for the maintenance. With shift of location to downstream elbows (elbow flange connection with pipes), which can be replaced within 3 to 4 hrs. This modification proposed thus reduces machine downtime (outage) and energy saved per outage for maintenance was found to be about 926 MWh. This modification proposed thus reduces machine downtime (outage) hence increase generation. Detail calculations and previous outage data for repair is presented in tabular form in APPENDIX I.

# CHAPTER FIVE: CONCLUSION AND RECOMMENDATION

## 5.1 Conclusions

The key findings of this thesis study are mentioned in the section below.

(i) To identify the erosion-prone location, photographs of the running elbow and the damaged elbow that had been disassembled were taken during the field visit. The lower side elbow extrados found significant deterioration (which is embedded with the headcover). It was also discovered by CFD modeling, which employed the McLaury erosion model and varying sediment concentrations from tested samples, that the erosion rate density rises in response to rising sediment concentrations and vice versa. Additionally, a field visit revealed that the leaks in the balancing pipes were most frequently noted during the wet season. Sediment concentration is, thus, one of the primary causes of erosion on material surfaces.

(ii) The results of the ANSYS simulation showed that the region of erosion and erosion rate density were both high at the same location as the highest thickness loss observed during the field visit. So, modeling and experiment results revealed an erosion-prone zone since they closely matched one another. Due to direct contact of sediment particles, erosion was observed to be greater in the elbow's outer curve, where the flow quickly changes from the inlet to the outlet. As a result, the outer curvature's surface erodes the most, but the inner curvature may suffer cavitation due to the created negative pressure.

(iii) The erosion rate density at different locations (locations of thickness measurement) from the simulation follows the same trend as the experimental results with a deviation (average error) of 69.58%.

(iv) When compared to the existing system, the proposed design exhibited an average 13.49% reduction in erosion rate density. With the relocation of the erosion-prone area to downstream elbows, which can be repaired/ replaced more quickly and easily than lower elbows (elbow embedded with headcover). The proposed system saved around 926 MWh of energy per maintenance outage as compared to the existing system. Thus, the proposed system decreases machine downtime, increasing generation.

## 5.2 Recommendations

The following recommendations can be suggested for further study

(i) A shape optimization study could be performed to further reduce the erosion rate density. Additionally, after erosion, the flow regime in the wall changes, creating a region of high local velocity and therefore low pressure that initiates the cavitation process. It is suggested to do more study utilizing CFD models and testing in order to properly understand the beginning of cavitation in Pressure balancing pipes.

(ii) From this study it was seen from CFD analysis that modification has potential to reduce machine outage contributing to increase in generation. It is recommended to CHEPS to experimentally trial the modification proposed and if found successful then implement it in their machine. Such modification of turbine parts also needs to be studied in other areas of erosion like turbine runner, guide vanes for minimizing erosion and maintaining higher efficiency for a longer operation period.

## REFRENCES


Andrews, D. R. (1981). An analysis of solid particle erosion mechanisms. *Journal of Physics D: Applied Physics*, *14*(11), 1979–1991. https://doi.org/10.1088/0022-3727/14/11/006

ANSYS Inc. (n.d.). *FLUENT 6.3 User's Guide - 22.5 Particle Erosion and Accretion Theory*. https://www.sharcnet.ca/Software/Fluent6/html/ug/node818.htm

ANSYS Inc. (2013). *ANSYS Fluent Theory Guide* (Release 15.0). http://www.pmt.usp.br/ACADEMIC/martoran/NotasModelosGrad/ANSYS

Aquaro, D., & Fontani, E. (2001). Erosion of Ductile and Brittle Materials. *Meccanica*, *36*(6), 651–661. https://doi.org/10.1023/A:1016396719711

Baidar, B., Chitrakar, S., Koirala, R., & Neopane, H. P. (2015). Selection of optimal number of francis runner blades for a sediment laden micro hydropower plant in Nepal. *International Journal of Fluid Machinery and Systems*, *8*(4), 294–303. https://doi.org/10.5293/IJFMS.2015.8.4.294

Bitter, J. G. A. (1963a). A study of erosion phenomena part I. *Wear*, *6*(1), 5–21. https://doi.org/10.1016/0043-1648(63)90003-6

Bitter, J. G. A. (1963b). A study of erosion phenomena: Part II. *Wear*, *6*(3), 169–190. https://doi.org/10.1016/0043-1648(63)90073-5

Brekke, H., Wu, Y. L., & Cai, B. Y. (2010). *Design of Hydraulic Machinery Working in Sand Laden Water*. 155–233. https://doi.org/10.1142/9781848160026_0004

Budiarti, novi yulia. (2020). *Sustainability (Switzerland)*, *4*(1), 1–9. https://pesquisa.bvsalud.org/portal/resource/en/mdl-20203177951%0Ahttp://dx.doi.org/10.1038/s41562-020-0887-9%0Ahttp://dx.doi.org/10.1038/s41562-020-0884-z%0Ahttps://doi.org/10.1080/13669877.2020.1758193%0Ahttp://sersc.org/journals/index.php/IJAST/article

Chongji. Zeng., Y.X., X., Jianbo, Z., Soo-Hwang, A., & Zhengwei, W. (2015). Numerical analysis of pelton turbine needle erosion characteristics. *Paiguan Jixie Gongcheng Xuebao/Journal of Drainage and Irrigation Machinery Engineering*, *33*(5), 407–411.

https://www.researchgate.net/publication/282983395_Numerical_analysis_of_pelton_turbine_needle_erosion_characteristics

Dahal, D. R., Chitrakar, S., Kapali, A., Thapa, B. S., & Neopane, H. P. (2019). Design of Spiral Casing of Francis Turbine for Micro Hydro Applications. *Journal of Physics: Conference Series*, *1266*(1). https://doi.org/10.1088/1742-6596/1266/1/012013

Eltvik Mette. (2013). Sediment erosion in Francis turbines. *Ph.D. Thesis*, *June*.

Finnie, I. (1960). Erosion of surfaces by solid particles. *Wear*, *3*(2), 87–103. https://doi.org/10.1016/0043-1648(60)90055-7

Finnie, I. (1972). Some observations on the erosion of ductile metals. *Wear*, *19*(1), 81–90. https://doi.org/10.1016/0043-1648(72)90444-9

Javaheri, V., Porter, D., & Kuokkala, V.-T. (2018). Slurry erosion of steel – Review of tests, mechanisms and materials. *Wear*, *408–409*, 248–273. https://doi.org/10.1016/J.WEAR.2018.05.010

Khan, R., Ya, H. H., Pao, W., & Khan, A. (2019). Erosion-corrosion of 30°, 60°, and 90° carbon steel elbows in a multiphase flow containing sand particles. *Materials*, *12*(23). https://doi.org/10.3390/ma122333898

Khan, R., Ya, H. H., Pao, W., Majid, M. A. A., Ahmed, T., Ahmad, A., Alam, M. A., Azeem, M., & Iftikhar, H. (2020). Effect of sand fines concentration on the erosion-corrosion mechanism of carbon steel 90◦ elbow pipe in slug flow. *Materials*, *13*(20), 1–16. https://doi.org/10.3390/ma13204601

Kleĭs, I. R. (Il′mar R., & Kulu, P. (2008). *Solid particle erosion : occurrence, prediction and control*. Springer.

Kosinska, A., Balakin, B. V., & Kosinski, P. (2020). Theoretical analysis of erosion in elbows due to flows with nano- and micro-size particles. *Powder Technology*, *364*, 484–493. https://doi.org/10.1016/j.powtec.2020.02.002

Lospa, A. M., Dudu, C., Ripeanu, R. G., & Dinita, A. (2019). CFD Evaluation of sand erosion wear rate in pipe bends used in technological installations. *IOP Conference Series: Materials Science and Engineering*, *514*(1). https://doi.org/10.1088/1757-899X/514/1/012009

Mazumder, Q. H., Zhao, S., & Ahmed, K. (2015). Effect of bend radius on magnitude and location of erosion in s-bend. *Modelling and Simulation in Engineering, 2015*. https://doi.org/10.1155/2015/930497

McLaury, B. S., Wang, J., Shirazi, S. A., Shadley, J. R., & Rybicki, E. F. (1997). Solid particle erosion in long radius elbows and straight pipes. In *Proceedings - SPE Annual Technical Conference and Exhibition: Vol. Pi* (pp. 977–986). https://doi.org/10.2523/38842-ms

Neilson, J. H., & Gilchrist, A. (1968). Erosion by a stream of solid particles. *Wear*, *11*(2), 111–122. https://doi.org/10.1016/0043-1648(68)90591-7

Neopane, H. P., Gunnar Dahlhaug, O., & Cervantes, M. (2011). Sediment Erosion in Hydraulic Turbines. *Global Journal of Researches in Engineering Mechanical and Mechanics Engineering , 6*, 17–26. https://pdfs.semanticscholar.org/f219/b5289d91874f8d13090063c34688ebebe978.pdf?_ga=2.265510923.564185937.1556240431-87428635.1550801047

Neopane, H. P., & Sujakhu, S. (2013). PARTICLE SIZE DISTRIBUTION AND MINERAL ANALYSIS OF SEDIMENTS IN NEPALESE HYDROPOWER PLANT: A CASE STUDY OF JHIMRUK HYDROPOWER PLANT. In *KATHMANDU UNIVERSITY JOURNAL OF SCIENCE, ENGINEERING AND TECHNOLOGY* (Vol. 9, Issue I). http://www.ku.edu.np/kusetjournal/vol9_no1/3_Hari_Prasad_Neopane_final.pdf

Oka, Y. I., Okamura, K., & Yoshida, T. (2005). Practical estimation of erosion damage caused by solid particle impact: Part 1: Effects of impact parameters on a predictive equation. *Wear*, *259*(1–6), 95–101. https://doi.org/10.1016/J.WEAR.2005.01.039

Oka, Y. I., & Yoshida, T. (2005). Practical estimation of erosion damage caused by solid particle impact: Part 2: Mechanical properties of materials directly associated with erosion damage. *Wear*, *259*(1–6), 102–109. https://doi.org/10.1016/J.WEAR.2005.01.040

Parsi, M., Najmi, K., Najafifard, F., Hassani, S., McLaury, B. S., & Shirazi, S. A. (2014). A comprehensive review of solid particle erosion modeling for oil and gas wells and pipelines applications. *Journal of Natural Gas Science and Engineering*,

*21*, 850–873. https://doi.org/10.1016/j.jngse.2014.10.001

Poudel, L., Thapa, B., Shrestha, B. P., Thapa, B. S., Shrestha, K. P., & Shrestha, N. K. (2012). Computational and experimental study of effects of sediment shape on erosion of hydraulic turbines. *IOP Conference Series: Earth and Environmental Science*, *15*(3), 32054. https://doi.org/10.1088/1755-1315/15/3/032054

Sinha, S. L., Dewangan, S. K., & Sharma, A. (2017). A review on particulate slurry erosive wear of industrial materials: In context with pipeline transportation of mineral−slurry. *Particulate Science and Technology*, *35*(1), 103–118. https://doi.org/10.1080/02726351.2015.1131792

Srinivasan, V., & Ph, D. (2014). *Simulating Erosion Using ANSYS Computational Fluid Dynamics*.

Zhang, F., Lv, Y., Gui, Z., & Wang, Z. (2021). Effect of the diameter of pressure-balance pipe on axial hydraulic thrust. *Journal of Marine Science and Engineering*, *9*(7). https://doi.org/10.3390/jmse9070724

Zhang, L., Zhou, J. W., Zhang, B., & Gong, W. (2020). Numerical investigation on the solid particle erosion in elbow with water–hydrate–solid flow. *Science Progress*, *103*(1). https://doi.org/10.1177/0036850419897245

# APPENDIX A: DRY WEIGHT OF SEDIMENT SAMPLE

Hydro Lab
IN COOPERATION WITH NTNU, NORWAY

HLPL/F/RSoLA/01

## RESULT SHEET OF LABORATORY ANALYSES

| | | | |
|---|---|---|---|
| Client: | Mr. Chiranjibi Acharya, Department of Mechanical and Aerospace Engineering, Pulchowk Campus, IOE, TU, Nepal | | |
| Project: | Chameliya Hydropower Project | | |
| Sampling location: | Project site | | |
| Sample provided by: | Client | | |
| Reporting date: | 30 August 2022 | Report no: | 263-8.L1_rev1 |

### Tests and number of analyses

| SN | Types of Test | | Qty | SN | Types of Test | | Qty |
|---|---|---|---|---|---|---|---|
| A. | Drying & weighing of filter paper with sediment | √ | 10 | B. | Particle size distribution (PSD) | √ | 5 |
| C. | Mineral content | √ | 5 | D. | Organic matters content | - | - |

### A. Results of dry weight of Suspended Sediment sample (filter paper sample)

| S. No. | Sample No. | Sampling date | Dish no. | Dry wt. of filter paper with dish (gm) | Dry wt. of filter paper with sediment + dish (gm) | Net wt. of sample (gm) |
|---|---|---|---|---|---|---|
| 1 | 7 | 03/05/2022 | 125 | 36.8476 | 37.2678 | 0.4202 |
| 2 | 8 | 13/05/2022 | 126 | 18.4374 | 18.9299 | 0.4925 |
| 3 | 4 | 23/05/2022 | 116 | 31.2356 | 32.8282 | 1.5926 |
| 4 | 3 | 03/06/2022 | 115 | 29.0467 | 31.5868 | 2.5401 |
| 5 | 10 | 13/06/2022 | 128 | 23.324 | 27.5863 | 4.2623 |
| 6 | 2 | 23/06/2022 | 114 | 31.0192 | 35.0647 | 4.0455 |
| 7 | 5 | 04/07/2022 | 117 | 30.9157 | 36.2244 | 5.3087 |
| 8 | 6 | 13/07/2022 | 124 | 28.935 | 32.9908 | 4.0558 |
| 9 | 9 | 23/07/2022 | 127 | 24.0798 | 26.4899 | 2.4101 |
| 10 | 1 | 02/08/2022 | 122 | 30.9195 | 32.9756 | 2.0561 |

## APPENDIX B: PSD GRAPH

Hydro Lab
IN COOPERATION WITH NTNU, NORWAY

HLPL/F/RSoLA/01

**B. Results of Particle Size Distribution (PSD)**

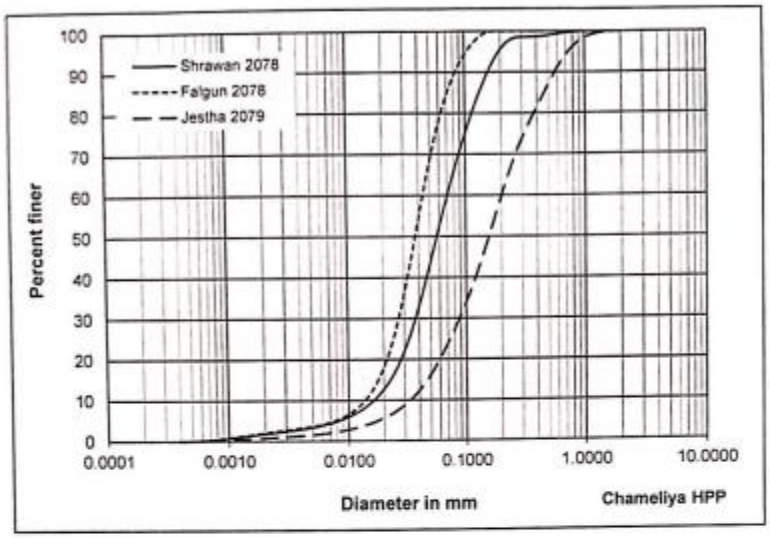


**Figure B- 1: PSD curves of the suspended sediment samples taken on Shrawan 2078, Falgun 2078 and Jestha 2079**

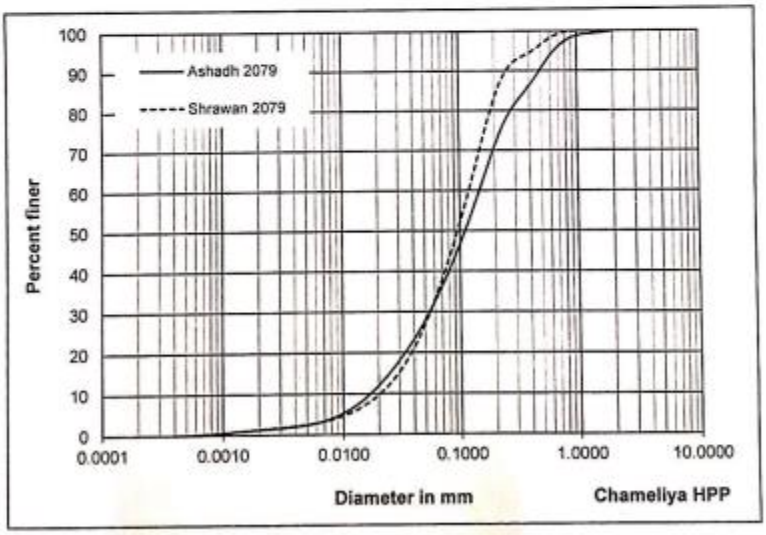


**Figure B- 2: PSD curves of the suspended sediment samples taken on Ashadh 2079 and Shrawan 2079**

HYDRO LAB PVT. LTD.

# APPENDIX C: MINERAL CONTENT ANALYSIS

Hydro Lab
IN COOPERATION WITH NTNU, NORWAY

HLPL/F/RSoLA/01

## C. Results of Mineral Content

**Table C-1: Shrawan 2078**

| Minerals | | Sample (%) | | | Average (%) | Hardness (Moh's scale) |
|---|---|---|---|---|---|---|
| | | 1 | 2 | 3 | | |
| Quartz | | 65 | 69 | 67 | 67 | 7 |
| Feldspar | | 2 | 3 | 1 | 2 | 6 |
| Mica | | 16 | 13 | 16 | 15 | 2-3 |
| Other | A | 1 | 1 | 1 | 1 | ≥ 5 |
| | B | 16 | 14 | 15 | 15 | < 5 |

**Table C-2: Falgun 2078**

| Minerals | | Sample (%) | | | Average (%) | Hardness (Moh's scale) |
|---|---|---|---|---|---|---|
| | | 1 | 2 | 3 | | |
| Quartz | | 68 | 64 | 66 | 66 | 7 |
| Feldspar | | 3 | 2 | 4 | 3 | 6 |
| Mica | | 14 | 15 | 13 | 14 | 2-3 |
| Other | A | 1 | 1 | 1 | 1 | ≥ 5 |
| | B | 14 | 18 | 16 | 16 | < 5 |

**Table C-3: Jestha 2079**

| Minerals | | Sample (%) | | | Average (%) | Hardness (Moh's scale) |
|---|---|---|---|---|---|---|
| | | 1 | 2 | 3 | | |
| Quartz | | 70 | 68 | 69 | 69 | 7 |
| Feldspar | | 2 | 2 | 2 | 2 | 6 |
| Mica | | 11 | 15 | 13 | 13 | 2-3 |
| Other | A | 1 | 1 | 1 | 1 | ≥ 5 |
| | B | 16 | 14 | 15 | 15 | < 5 |

**Table C-4: Ashadh 2079**

| Minerals | | Sample (%) | | | Average (%) | Hardness (Moh's scale) |
|---|---|---|---|---|---|---|
| | | 1 | 2 | 3 | | |
| Quartz | | 68 | 64 | 72 | 68 | 7 |
| Feldspar | | 1 | 3 | 2 | 2 | 6 |
| Mica | | 14 | 14 | 11 | 13 | 2-3 |
| Other | A | 1 | 1 | 1 | 1 | ≥ 5 |
| | B | 16 | 18 | 14 | 16 | < 5 |

**Table C-5: Shrawan 2079**

| Minerals | | Sample (%) | | | Average (%) | Hardness (Moh's scale) |
|---|---|---|---|---|---|---|
| | | 1 | 2 | 3 | | |
| Quartz | | 68 | 67 | 69 | 68 | 7 |
| Feldspar | | 2 | 2 | 2 | 2 | 6 |
| Mica | | 12 | 15 | 12 | 13 | 2-3 |
| Other | A | 1 | 1 | 1 | 1 | ≥ 5 |
| | B | 17 | 15 | 16 | 16 | < 5 |

**Note:**

Other A: Tourmaline, Garnet, hornblende and Olivine
Other B: Carbonate (~14 %), Clay, Organic matters, and up to 2% unidentified mineral and rock fragments (slate)

HYDRO LAB PVT. LTD. NEPAL

## APPENDIX D: EROSION RATE DENSITY WITH DIFFERENT SEDIMENT CONCENTRATION

| Date | Mass flow rate of water (kg/s) | Density of water ($kg/m^3$) | Sediment concentration (ppm) | Calculated mass flow rate of sand (kg/s) | Maximum Erosion rate density from simulation ($kg/m^2s$) |
|---|---|---|---|---|---|
| May 3 | 77.84 | 998.20 | 420.20 | 0.0328 | 7.51420E-06 |
| May 13 | 77.84 | 998.20 | 492.50 | 0.0384 | 8.57670E-06 |
| May 23 | 77.84 | 998.20 | 1592.60 | 0.1242 | 2.97017E-05 |
| June 3 | 77.84 | 998.20 | 2540.10 | 0.1981 | 5.04865E-05 |
| June 13 | 77.84 | 998.20 | 4262.30 | 0.3324 | 9.19843E-05 |
| June 23 | 77.84 | 998.20 | 4045.50 | 0.3155 | 7.43161E-05 |
| July 4 | 77.84 | 998.20 | 5308.70 | 0.4140 | 1.19090E-04 |
| July 13 | 77.84 | 998.20 | 4055.80 | 0.3163 | 7.44253E-05 |
| July 23 | 77.84 | 998.20 | 2410.10 | 0.1879 | 4.61854E-05 |
| August 2 | 77.84 | 998.20 | 2056.10 | 0.1603 | 4.18667E-05 |
| Average | 77.84 | 998.20 | 2718.39 | 0.2120 | 5.80483E-05 |

## APPENDIX E: COMPARISON OF EROSION RATE DENSITY AT DIFFERENT LOCATIONS

| Position | Measured thickness (mm) | Loss in thickness (mm) | Erosion rate density from experiment ($kg/m^2s$) | Erosion rate density from simulation ($kg/m^2s$) | Error % |
|---|---|---|---|---|---|
| 1' | 9.08 | 0.92 | 9.50051E-07 | 1.00346E-06 | 5.62% |
| 2' | 8.16 | 1.84 | 1.90010E-06 | 1.05794E-06 | 44.32% |
| 3' | 7.04 | 2.96 | 3.05669E-06 | 2.09893E-06 | 31.33% |
| 4' | 4.50 | 5.50 | 5.67966E-06 | 8.16256E-06 | 43.72% |
| 5' | 2.20 | 7.80 | 8.05478E-06 | 9.18934E-06 | 14.09% |
| 6' | 2.50 | 7.50 | 7.74498E-06 | 1.01555E-05 | 31.12% |
| 7' | 1.60 | 8.40 | 8.67438E-06 | 1.51256E-05 | 74.37% |
| 8' | 1.70 | 8.30 | 8.57112E-06 | 2.57234E-05 | 200.12% |
| 9' | 1.50 | 8.50 | 8.77765E-06 | 2.58971E-05 | 195.03% |
| A | 9.04 | 0.96 | 9.91358E-07 | 1.22125E-06 | 23.19% |
| B | 8.54 | 1.46 | 1.50769E-06 | 1.26374E-06 | 16.18% |
| C | 7.04 | 2.96 | 3.05669E-06 | 2.13137E-06 | 30.27% |
| D | 6.50 | 3.50 | 3.61433E-06 | 1.03283E-06 | 71.42% |
| E | 3.56 | 6.44 | 6.65036E-06 | 6.91243E-06 | 3.94% |
| F | 3.02 | 6.98 | 7.20800E-06 | 1.12359E-05 | 55.88% |
| G | 1.26 | 8.74 | 9.02549E-06 | 2.01434E-05 | 123.18% |
| H | 1.20 | 8.80 | 9.08745E-06 | 2.12276E-05 | 133.59% |
| I | 1.80 | 8.20 | 8.46785E-06 | 2.13577E-05 | 152.22% |
| A' | 9.08 | 0.92 | 9.50051E-07 | 1.24729E-06 | 31.29% |
| B' | 9.14 | 0.86 | 8.88092E-07 | 1.27376E-06 | 43.43% |
| C' | 6.50 | 3.50 | 3.61433E-06 | 2.02142E-06 | 44.07% |
| D' | 5.80 | 4.20 | 4.33719E-06 | 2.05223E-06 | 52.68% |
| E' | 4.08 | 5.92 | 6.11337E-06 | 6.93564E-06 | 13.45% |
| F' | 1.40 | 8.60 | 8.88092E-06 | 1.12416E-05 | 26.58% |
| G' | 1.42 | 8.58 | 8.86026E-06 | 2.04302E-05 | 130.58% |
| H' | 1.36 | 8.64 | 8.92222E-06 | 2.13527E-05 | 139.32% |
| I' | 1.50 | 8.50 | 8.77765E-06 | 2.17433E-05 | 147.71% |
| Average | 4.46 | 5.54 | 5.71714E-06 | 1.01199E-05 | 69.58% |

## APPENDIX F: MASS FLOW RATE FOR PROPOSED DESIGN

| Date | Mass flow rate of water (kg/s) | Density of water ($kg/m^3$) | Sediment concentration (ppm) | Mass flow rate of sand (kg/s) |
|---|---|---|---|---|
| May 3 | 49.96 | 998.20 | 420.20 | 0.0210 |
| May 13 | 49.96 | 998.20 | 492.50 | 0.0246 |
| May 23 | 49.96 | 998.20 | 1592.60 | 0.0797 |
| June 3 | 49.96 | 998.20 | 2540.10 | 0.1271 |
| June 13 | 49.96 | 998.20 | 4262.30 | 0.2133 |
| June 23 | 49.96 | 998.20 | 4045.50 | 0.2025 |
| July 4 | 49.96 | 998.20 | 5308.70 | 0.2657 |
| July 13 | 49.96 | 998.20 | 4055.80 | 0.2030 |
| July 23 | 49.96 | 998.20 | 2410.10 | 0.1206 |
| August 2 | 49.96 | 998.20 | 2056.10 | 0.1029 |
| Average | 49.96 | 998.20 | 2718.39 | 0.1361 |

## APPENDIX G: COMPARISON OF RESULTS (FIELD & SIMULATION) OF EXISTING SYSTEM

### i. Outer curvature surface of elbow

| Position | Loss in thickness (mm) | Erosion density from experiment ($kg/m^2s$) | Erosion density from simulation ($kg/m^2s$) | Error % |
|---|---|---|---|---|
| 1' | 0.92 | 9.50051E-07 | 1.00346E-06 | 5.62% |
| 2' | 1.84 | 1.90010E-06 | 1.05794E-06 | 44.32% |
| 3' | 2.96 | 3.05669E-06 | 2.09893E-06 | 31.33% |
| 4' | 5.50 | 5.67966E-06 | 8.16256E-06 | 43.72% |
| 5' | 7.80 | 8.05478E-06 | 9.18934E-06 | 14.09% |
| 6' | 7.50 | 7.74498E-06 | 1.01555E-05 | 31.12% |
| 7' | 8.40 | 8.67438E-06 | 1.51256E-05 | 74.37% |
| 8' | 8.30 | 8.57112E-06 | 2.57234E-05 | 200.12% |
| 9' | 8.50 | 8.77765E-06 | 2.58971E-05 | 195.03% |
| Average | 5.75 | 5.93438E-06 | 1.09349E-05 | 71.08% |

### ii. Front side wall of elbow

| Position | Loss in thickness (mm) | Erosion density from experiment ($kg/m^2s$) | Erosion density from simulation ($kg/m^2s$) | Error % |
|---|---|---|---|---|
| A | 0.96 | 9.91358E-07 | 1.22125E-06 | 23.19% |
| B | 1.46 | 1.50769E-06 | 1.26374E-06 | 16.18% |
| C | 2.96 | 3.05669E-06 | 2.13137E-06 | 30.27% |
| D | 3.50 | 3.61433E-06 | 1.03283E-06 | 71.42% |
| E | 6.44 | 6.65036E-06 | 6.91243E-06 | 3.94% |
| F | 6.98 | 7.20800E-06 | 1.12359E-05 | 55.88% |
| G | 8.74 | 9.02549E-06 | 2.01434E-05 | 123.18% |
| H | 8.80 | 9.08745E-06 | 2.12276E-05 | 133.59% |
| I | 8.20 | 8.46785E-06 | 2.13577E-05 | 152.22% |
| Average | 5.34 | 5.51213E-06 | 9.61402E-06 | 74.42% |

### iii. Back side wall of elbow

| Position | Loss in thickness (mm) | Erosion density from experiment ($kg/m^2s$) | Erosion density from simulation ($kg/m^2s$) | Error % |
|---|---|---|---|---|
| A' | 0.92 | 9.50051E-07 | 1.24729E-06 | 31.29% |
| B' | 0.86 | 8.88092E-07 | 1.27376E-06 | 43.43% |
| C' | 3.50 | 3.61433E-06 | 2.02142E-06 | 44.07% |
| D' | 4.20 | 4.33719E-06 | 2.05223E-06 | 52.68% |
| E' | 5.92 | 6.11337E-06 | 6.93564E-06 | 13.45% |
| F' | 8.60 | 8.88092E-06 | 1.12416E-05 | 26.58% |
| G' | 8.58 | 8.86026E-06 | 2.04302E-05 | 130.58% |
| H' | 8.64 | 8.92222E-06 | 2.13527E-05 | 139.32% |
| I' | 8.50 | 8.77765E-06 | 2.17433E-05 | 147.71% |
| Average | 5.52 | 5.70490E-06 | 9.81090E-06 | 69.90% |

## APPENDIX H: COMPARISON OF RESULTS OF EXISTING AND PROPOSED SYSTEM

| Date | Sediment concentration (ppm) | Maximum Erosion rate density of existing system ($kg/m^2s$) | Maximum Erosion rate density of proposed design ($kg/m^2s$) | Error % |
|---|---|---|---|---|
| May 3 | 420.20 | 7.51420E-06 | 6.73386E-06 | 10.38% |
| May 13 | 492.50 | 8.57670E-06 | 9.87567E-06 | -15.15% |
| May 23 | 1592.60 | 2.97017E-05 | 2.25411E-05 | 24.11% |
| June 3 | 2540.10 | 5.04865E-05 | 3.96211E-05 | 21.52% |
| June 13 | 4262.30 | 9.19843E-05 | 7.06060E-05 | 23.24% |
| June 23 | 4045.50 | 7.43161E-05 | 6.85409E-05 | 7.77% |
| July 4 | 5308.70 | 1.19090E-04 | 8.40158E-05 | 29.45% |
| July 13 | 4055.80 | 7.44253E-05 | 6.40305E-05 | 13.97% |
| July 23 | 2410.10 | 4.61854E-05 | 4.48428E-05 | 2.91% |
| August 2 | 2056.10 | 4.18667E-05 | 3.48653E-05 | 16.72% |
| Average | 2718.39 | 5.44147E-05 | 4.45673E-05 | 13.49% |

## APPENDIX I: ENERGY LOSS CALCULATION DURING MAINTENANCE OUTAGE

### i. Calculation of per Unit per hour designed capacity (MW):

| Month | Design energy (MWh) | Per Unit design energy (MWh) | Per Unit per hour designed capacity (MW) |
|---|---|---|---|
| Baisakh | 11,970.00 | 5,985.00 | 8.31 |
| Jestha | 17,570.00 | 8,785.00 | 12.20 |
| Ashad | 21,225.00 | 10,612.50 | 14.74 |
| Shrawan | 21,570.00 | 10,785.00 | 14.98 |
| Bhadra | 21,225.00 | 10,612.50 | 14.74 |
| Ashwin | 21,225.00 | 10,612.50 | 14.74 |
| Kartik | 19,110.00 | 9,555.00 | 13.27 |
| Mangsir | 14,285.00 | 7,142.50 | 9.92 |
| Paush | 10,695.00 | 5,347.50 | 7.43 |
| Magh | 8,445.00 | 4,222.50 | 5.86 |
| Fagun | 7,875.00 | 3,937.50 | 5.47 |
| Chaitra | 9,005.00 | 4,502.50 | 6.25 |

### ii. Energy loss (MWh) during maintenance of lower elbow (elbow embedded with headcover):

| Date | Generating Unit | Maintenance time | Per Unit per hour designed capacity (MW) | Energy loss (MWh) |
|---|---|---|---|---|
| 5/12/2078 | Unit 2 | 24:00:00 | | |
| 5/13/2078 | | 24:00:00 | | |
| 5/14/2078 | | 16:55:00 | | |
| Total | | 64:55:00 | 14.74 | 956.84 |
| 7/9/2078 | Unit 2 | 15:00:00 | | |
| 7/10/2078 | | 24:00:00 | | |
| 7/11/2078 | | 24:00:00 | | |
| 7/12/2078 | | 17:47:00 | | |

| | | | | |
|---|---|---|---|---|
| Total | | 80:47:00 | 13.27 | 1072.06 |
| 4/10/2079 | | 17:30:00 | | |
| 4/11/2079 | | 24:00:00 | | |
| 4/12/2079 | | 19:00:00 | | |
| Total | | 60:30:00 | 14.98 | 906.24 |
| Average | | 68:44:00 | 14.33 | 978.38 |

**iii. Energy loss during replacement of downstream elbows/ pipes (elbows having flange connection with pipe):**

| Date | Generating Unit | Maintenance | Per Unit per hour designed capacity (MW) | Energy loss (MWh) |
|---|---|---|---|---|
| 4/29/2076 | Unit 2 | 5:11:00 | 14.98 | 77.64 |
| 4/32/2076 | Unit 1 | 4:43:00 | 14.98 | 70.65 |
| 5/6/2076 | Unit 1 | 4:53:00 | 14.74 | 71.98 |
| | | 2:25:00 | 14.74 | 35.62 |
| 5/7/2076 | | 1:13:00 | 14.74 | 17.93 |
| 5/9/2076 | | 3:23:00 | 14.74 | 49.87 |
| 5/9/2076 | Unit 2 | 4:23:00 | 14.74 | 64.61 |
| 6/4/2076 | Unit 1 | 2:43:00 | 14.74 | 40.04 |
| 6/5/2076 | | 4:39:00 | 14.74 | 68.54 |
| 7/6/2076 | Unit 1 | 1:50:00 | 13.27 | 24.33 |
| 7/7/2076 | | 1:04:00 | 13.27 | 14.16 |
| | | 2:21:00 | 13.27 | 31.19 |
| 2/18/2077 | Unit 2 | 1:58:00 | 12.20 | 24.00 |
| 3/24/2077 | Unit 1 | 2:04:00 | 14.74 | 30.46 |
| 3/30/2077 | | 2:06:00 | 14.74 | 30.95 |
| 3/30/2077 | Unit 2 | 2:50:00 | 14.74 | 41.76 |
| 4/23/2077 | Unit 2 | 2:32:00 | 14.98 | 37.95 |
| 6/2/2077 | Unit 1 | 4:21:00 | 14.74 | 64.12 |
| 6/17/2077 | | 4:23:00 | 14.74 | 64.61 |

| | | | | |
|---|---|---|---|---|
| 6/4/2077 | Unit 2 | 2:30:00 | 14.74 | 36.85 |
| 6/6/2077 | | 2:24:00 | 14.74 | 35.38 |
| 7/17/2077 | Unit 1 | 4:29:00 | 13.27 | 59.50 |
| 7/25/2077 | | 5:28:00 | 13.27 | 72.55 |
| 2/30/2078 | Unit 1 | 2:56:00 | 12.20 | 35.79 |
| 2/12/2078 | Unit 2 | 6:33:00 | 12.20 | 79.92 |
| 3/8/2078 | Unit 1 | 4:48:00 | 14.74 | 70.75 |
| 3/9/2078 | | 2:17:00 | 14.74 | 33.66 |
| 3/12/2078 | | 6:28:00 | 14.74 | 95.32 |
| 3/20/2078 | | 2:27:00 | 14.74 | 36.11 |
| 3/2/2078 | Unit 2 | 5:35:00 | 14.74 | 82.30 |
| 3/11/2078 | | 6:40:00 | 14.74 | 98.26 |
| 4/3/2078 | Unit 1 | 4:22:00 | 14.98 | 65.41 |
| Average | | 3:37:28 | 14.30 | 51.94 |
| Energy save during single maintenance outage (average of ii. – average of iii.) | | | | 926.44 MWh |

## APPENDIX J: PHOTOGRAPH

Leakage from elbow (embedded with headcover)

Erosion pattern in internal surface of elbow

Dismantalled elbow during overhauling

Elbow repair by welding

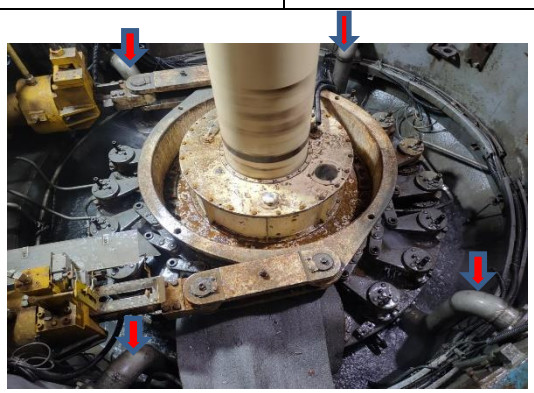

Headcover with PBP